Constitutive model with a concept of plastic rebound for expansive soils

Tachibana, Shinya

Ito, Shinji

Iizuka, Atsushi

(Citation)
Soils and Foundations,60(1):179-197

(Issue Date)
2020-02

(Resource Type)
journal article

(Version)
Version of Record

HOSTED BY
ELSEVIER
Available online at www.sciencedirect.com
ScienceDirect
Soils and Foundations 60 (2020) 179–197
www.elsevier.com/locate/sandf

Technical Paper

Constitutive model with a concept of plastic rebound for expansive soils

Shinya Tachibana [a,*], Shinji Ito [b], Atsushi Iizuka [a]

[a] Research Center for Urban Safety and Security, Kobe University, Japan
[b] Graduate School of Engineering Faculty of Engineering, Kobe University, Japan

Received 26 July 2019; received in revised form 22 January 2020; accepted 27 February 2020
Available online 2 April 2020

Abstract

This study examines the applicability of an elasto-plastic constitutive model with the concept of plastic rebound to describe the mechanical behaviour of expansive soils. The constitutive model can be characterized by an elliptical yield locus which is analogous to the modified Cam-clay model, but does not pass the origin of the effective stress space. In addition to the intrinsic normal consolidation line, the plastic rebound line is newly defined in order to describe a hardening law which allows the prediction of plastic swelling upon unloading. Through analytical investigations, the paper shows that the constitutive model can effectively predict not only the volume changes, but also the effective stress paths, i.e., K_0-values, for both consolidation and swelling in axial and radial problems, despite it being a simple modification. Also presented here are comparisons between the results of a simulation and laboratory tests on expansive soils in order to verify the applicability of the developed constitutive model.

Keywords: Expansive soil; Bentonite; Swelling; Plastic rebound; Critical state theory

1. Introduction

The existence of expansive soils at a construction site is sometimes considered a problem for soils with characteristics that make them prone to large volume changes. The assessment and prediction of the mechanical behaviour of expansive soils have become matters of importance in geotechnical engineering for the purpose of mitigating geotechnical hazards such as heaving (Jones and Jefferson, 2012). On the other hand, compacted bentonite or bentonite-based materials, being classified as expansive soils but having controlled quality, are expected to be used as buffers, backfill and closures in repository systems for nuclear waste by taking advantage of the above characteristics, i.e., low permeability, high swelling and high radionuclide retardation capacities (Pusch, 1979; Yong et al., 1986; Villar and Lloret, 2004; Komine and Watanabe, 2010; Cui, 2017). One of the most significant and common functions required among design concepts for bentonite barriers is the swelling capacity which allows for the filling and sealing of cavities or gaps against other repository components. Once a repository facility is closed, ground water will infiltrate the bentonite barrier through the surrounding host rock, which brings about the swelling of the bentonite. In the assessment of the long-term safety of repository systems, changes not only in dry density, but also in the stress components that would affect the performance of the designed barrier, must be quantitatively predicted. This leads to the need for a numerical method that can solve initial and boundary problems with a sound constitutive model that enables a description of the mechanical behaviours of bentonite.

Peer review under responsibility of The Japanese Geotechnical Society.
* Corresponding author.
E-mail address: stachi@people.kobe-u.ac.jp (S. Tachibana).

https://doi.org/10.1016/j.sandf.2020.02.007

A typical mechanical characteristic of expansive soils, including bentonite even under a saturated condition, is the large swelling that is seen to occur upon unloading in oedometer tests. It would be appropriate to assume that the large swelling of smectite-rich clay, such as bentonite, is caused by microstructural changes (Gens and Alonso, 1992; Yong, 1999; Cui et al., 2002a). In fact, it has become clear, for example, through mercury intrusion porosimeter tests, that compacted bentonite can have a bimodal pore size distribution (Pusch, 1982; Romero and Simms, 2008), indicating the presence of two kinds of dominant pores that are different in form, namely, inter-aggregate pores (or micro pores) and intra-aggregate pores (or macro pores), and that the double structure associated with these two pore levels will evolve along with mechanical, hydraulic and chemical actions (Cui et al., 2002b; Lloret et al., 2003; Hoffmann et al., 2007; Seiphoori et al., 2014; Manca et al., 2016). The appearance of non-negligible unload-reload loops in the stress-strain relation is also characteristic of expansive soils. According to the experimental results, clear loops can be observed on saturated bentonite (Börgesson et al., 1996; Namikawa and Sugano, 1997a; Sasakura et al., 2003) and on saturated bentonite-sand mixtures (Mitachi, 2008; Tong and Yin, 2011). Recently, Cui et al. (2013) suggested that the loops could be attributed to the competition between the mechanical and the physical-chemical effects on the microstructural changes. Some experimental studies (Börgesson et al., 1996; Sasakura et al., 2003; Dueck et al., 2016) have measured the radial or lateral stress changes even in oedometer tests, which are of great use for gaining a detailed understanding of the stress paths during swelling and for developing a constitutive model for application to multi-dimensional problems.

It is also well known that such swelling upon unloading, which is far from being purely elastic and can be seen not only for bentonite, but also for medium and high plasticity clays, induces the deterioration of the mechanical properties. Calabresi and Scarpelli (1985) found a remarkable difference in undrained shear strength between consolidated and swelled-reconsolidated samples of Tobi and Ancona clays. Takahashi et al. (2005) also reported that the swelling history affects the shear stiffness of London clay. It is also thought that swelling is due to a breakdown of the diagenetic bonds or a loss of cementation between particles that formed in the past (Terzaghi, 1936; Bjerrum, 1967).

From a microscopic viewpoint, although there is a variety of different mechanisms, depending on the material, it is possible to find the similarity whereby the swelling upon unloading is not a purely elastic response, but involves a certain plastic component, for the purpose of describing the stress-strain relations from the macro perspective. In fact, such volume changes have been phenomenologically interpreted in terms of reverse plasticity or plastic rebound (Parry and Amerasinghe, 1973; Amerashinghe and Kraft, 1983). That concept is associated with the hypothesis whereby the material loses its memory of the hardening it acquired in its past stress history. Carter et al. (1982) attempted to extend the critical state theory with their idea that the yield locus shrinks even due to elastic unloading in order to describe the behaviour of soils under repeated loading.

This study proposes an elasto-plastic constitutive model with the concept of plastic rebound in a simple, but original, form which does not violate the consistency condition, bearing in mind the prediction of the mechanical behaviour of expansive soils. The applicability and limitations of the constitutive model are then examined through analytical investigations of consolidation and swelling in axial and radial problems, since it is essentially required that the changes in axial and radial effective stresses be predicted depending on the direction of swelling, as well as volume changes, when assessing the performance of a repository system involving a bentonite buffer. The model is assumed to possess a single yield locus which is analogous to the modified Cam-clay model (Roscoe and Burland, 1968), but not passing the origin of the effective stress space. Since it is permissible to change not only the size of the yield locus, but also its location in the effective stress space associated with the occurrence of plastic volume change, the model may be categorized as a kinematic and isotropic hardening one (e.g., Mroz, 1967). However, a linkage is assumed between the evolutions of size and location in order to simplify the model structure and to reduce the number of material parameters to be specified. The applicability of the proposed constitutive model is further verified through comparisons of the results of a simulation and laboratory tests.

The paper focuses on the mechanical behaviour under the saturated condition in which the soil pores are ideally filled with water, even while recognizing the essentiality of the constitutive model that encompasses both saturated and unsaturated conditions, including their transitions, in order to address the problem of expansive soils as many studies have already done (e.g., Alonso and Gens, 1999; Sun and Sun, 2012; Takayama et al., 2017). As this paper only deals with effective stresses, the dash which is conventionally used to denote effective stress is omitted for the sake of the simplicity of the notational system. The infinitesimal small strain in the constitutive modelling is also considered, and compression is adopted as positive for both stresses and strains according to the convention of soil mechanics.

2. Elasto-plastic constitutive model with the concept of plastic rebound

The yield function adopted in this study is given as follows:

$$f = f(p, q, p_c, p_s) = \frac{q^2}{\tilde{M}^2} + (p - p_s)(p - p_c) = 0; \quad p_s < p_c \tag{1}$$

where p and q are the effective mean stress and the stress deviator defined, respectively, by

$$p = \frac{1}{3}\mathrm{tr}\boldsymbol{\sigma}, q = \frac{3}{2}\| \mathbf{s} \|; \ \mathbf{s} = \boldsymbol{\sigma} - p\mathbf{1} \tag{2}$$

in which $\boldsymbol{\sigma}$ is the effective stress tensor with deviatoric component $\mathbf{s}$. As depicted in Fig. 1, the yield locus is an ellipsoid of the modified Cam-clay model with ellipticity $\tilde{M}$, i.e., the ratio of major axis to minor axis, while its size F along the p axis is determined by the difference between two state variables, p_s and p_c, in the form

$$F = p_c - p_s > 0. \tag{3}$$

Variable p_c is a hardening parameter, analogous to the preconsolidation pressure, which defines the yield stress due to isotropic loading, whereas variable p_s is a hardening parameter which defines the yield stress due to isotropic unloading. When $p_s = 0$, Eq. (1) results in the yield function of the modified Cam-clay model itself, which implies that ellipticity $\tilde{M}$ is coincident with critical state parameter M; otherwise, the relationship between $\tilde{M}$ and M depends on the ratio of p_c to p_s. The similar yield function of Eq. (1) can be applied by setting the smaller variable p_s to be negative when the tensile yield strength is taken into consideration (e.g., Hashiguchi and Mase, 2007; Suebsuk et al., 2011), although this paper deals with only the case where both p_c and p_s are positive so that yielding of the material occurs only in the positive region of effective stress.

Assuming that the associated flow rule is applied, the top of the elliptical yield locus stands for the critical state because the corresponding stress state satisfies the condition such that $\partial f/\partial p = 0$. Thus, in terms of material constant M, ellipticity $\tilde{M}$ can be written as

$$\tilde{M} = (1 + 2\zeta)M \tag{4}$$

where ζ is, in general, the state variable denoting the position of the current yield locus against its size F. Without the contradiction of Eq. (3), the two hardening parameters can be expressed by

$$p_c = (1 + \zeta)F \text{ and } p_s = \zeta F. \tag{5}$$

In addition, the slope of a tangential line to the current yield locus, which passes through the origin of the effective stress space, is given by

$$\bar{M} = \frac{1 + 2\zeta}{2\sqrt{\zeta(1 + \zeta)}}M. \tag{6}$$

It is noted that $\bar{M}$ becomes undefined for the modified Cam-clay model ($\zeta = 0$) since the tangent line is vertical.

There is a choice in defining the growth/decay of p_c and p_s independently in terms of a strain-like hardening parameter, so as not to violate Eq. (3), which allows the model to describe the changes not only in the size and the position, but also in the shape of a yield locus. Although such a model is attractive from the viewpoint of its predictive capability and variety, it will require the determination of individual parameters for each hardening law. Thus, for the sake of simplicity, this study considers a linkage between p_c and p_s with a bold assumption that ζ is a material constant ($\zeta \geqslant 0$). Consequently, the yield function (1) can be written in terms of F as

$$f = f(p, q, F) = \frac{q^2}{\tilde{M}^2} + (p - \zeta F)\{p - (1 + \zeta)F\} = 0. \tag{7}$$

It is therefore obvious from Eqs. (4) and (6) that both $\tilde{M}$ and $\bar{M}$ become constant, no matter how the hardening/softening of the material occurs. Fig. 2 shows the relationship between critical state parameter M and ellipticity $\tilde{M}$ for a number of values for ζ. If the value for ζ is larger, the shape of the yield locus becomes vertically longer in the p-q stress space, even for lower values of critical state parameter M. On the other hand, the constant $\bar{M}$ stands for the slope of a boundary line limiting the admissible

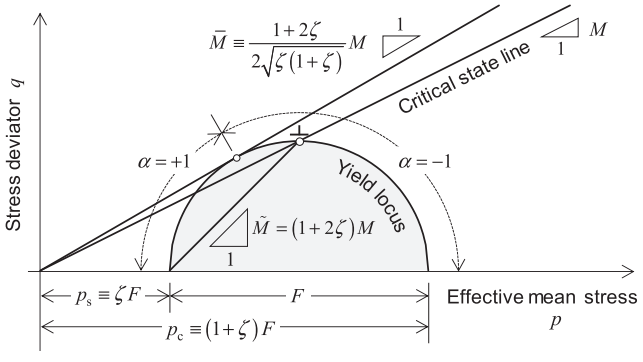

Fig. 1. Ellipsoid yield locus of modified Cam-clay model with concept of plastic rebound.

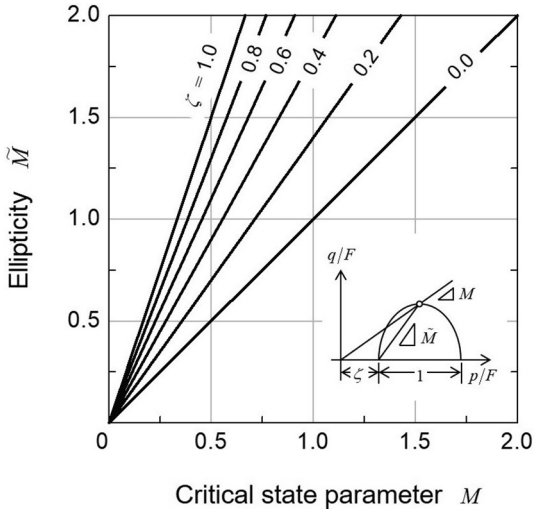

Fig. 2. Relationship between critical state parameter M and ellipticity $\tilde{M}$ for a number of values of ζ.

state of effective stress. Only when $\zeta = 0$, this line corresponds to the q-axis, and then its slope $\bar{M}$ becomes undefined as stated above.

Fig. 3(a) and (b) show the changes in the yield loci along the line with a slope $\bar{M}$ with plastic hardening and plastic softening, respectively. As seen in this figures, the material can yield not only on the wet side, where $\partial f/\partial p > 0$, but also on the dry side, where $\partial f/\partial p < 0$, even upon isotropic unloading, which causes a shrinkage of the yield loci and coordinated decreases in p_c and p_s. This is certainly a response that Calabresi and Scarpelli (1985) expressed by the words 'loss of memory' accompanied with plastic swelling for heavily overconsolidated clays. Kobayashi et al. (2007) also gave a similar interpretation of the yield characteristics of saturated bentonite based on the experimental fact that the yield stress upon reloading became much smaller than the preconsolidation pressure (i.e., the previous maximum stress) once the material underwent large swelling due to unloading in oedometer consolidation. Therefore, in a strict sense, it may be inadequate to refer to p_c as 'preconsolidation pressure', since it can decrease through swelling history, although the present study continues to use this terminology following the usual practice.

Fig. 4 shows the idealization of the responses under the isotropic stress condition and the corresponding changes in plastic volumetric strain to define the hardening law. The variations in void ratio e with respect to the logarithm of effective mean stress p are conventionally modeled as the normal consolidation line (NCL) for the elasto-plastic loading state and the 'elastic' swelling line (ESL) for the elastic state. Both of them are assumed to be linear with slope λ, called the compression index, and with slope κ, called the 'elastic' swelling index. A change in void ratio

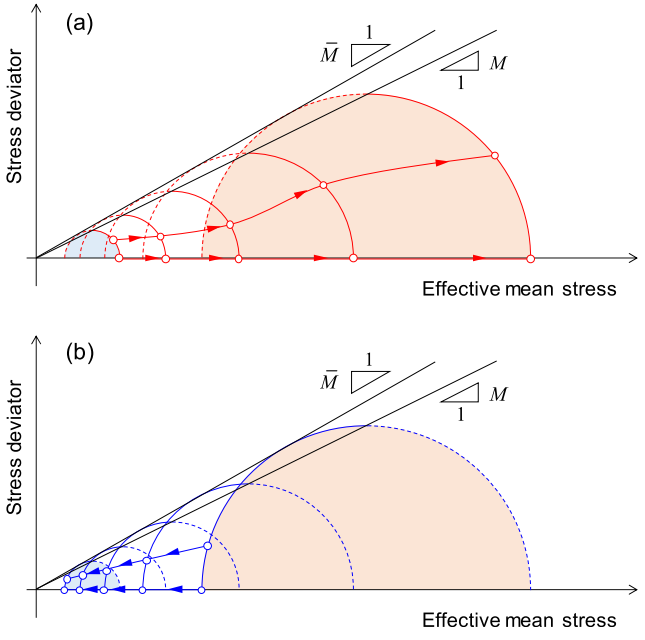

Fig. 3. Changes in yield loci along line with slope $\bar{M}$ with (a) plastic hardening and (b) plastic softening.

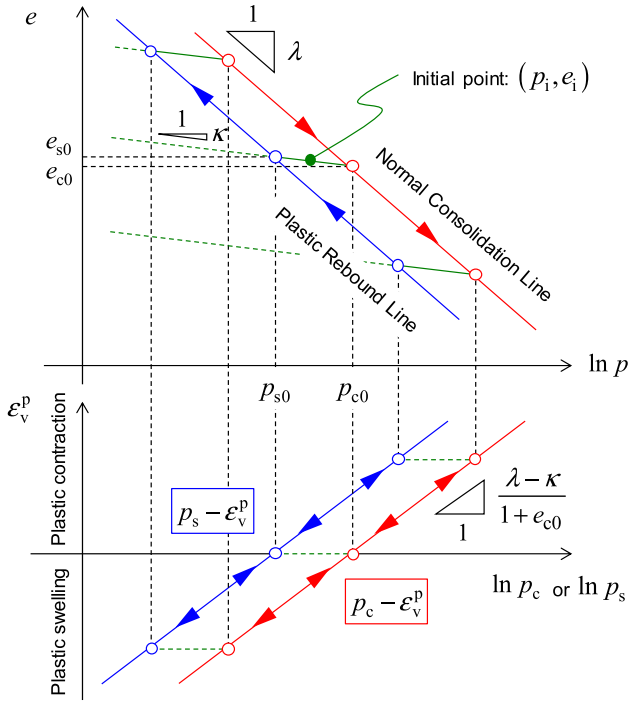

Fig. 4. Idealization of responses under isotropic stress condition and corresponding changes in plastic volumetric strain.

from the initial point (p_i, e_i) where the material has been elastically unloaded from the point (p_{c0}, e_{c0}) to the current point (p, e) elastically unloaded from the point (p_c, e_c) on the NCL can be expressed as

$$\begin{aligned}\Delta e = e - e_i &= (e - e_c) + (e_c - e_{c0}) + (e_{c0} - e_i)\\ &= -\kappa \ln \frac{p}{p_c} - \lambda \ln \frac{p_c}{p_{c0}} - \kappa \ln \frac{p_{c0}}{p_i}\\ &= -(\lambda - \kappa) \ln \frac{p_c}{p_{c0}} - \kappa \ln \frac{p}{p_i}.\end{aligned} \tag{8}$$

Since the first and second terms on the right-hand side of Eq. (8) are the plastic and elastic parts, respectively, of the void ratio change, the corresponding plastic and elastic volumetric strains are formulated, respectively, as

$$\varepsilon_v^p = \frac{\lambda - \kappa}{1 + e_{c0}} \ln \frac{p_c}{p_{c0}} \tag{9}$$

and

$$\varepsilon_v^e = \frac{\kappa}{1 + e_{c0}} \ln \frac{p}{p_i}, \tag{10}$$

provided that e_{c0} is a reference void ratio at the onset of plastic volumetric strain.

On the other hand, recalling that yielding of the material can occur upon unloading, another line for the elasto-plastic unloading state can be additionally defined on the $e - \ln p$ plane. This line, named the plastic rebound line (PRL) after the expression by Amerashinghe and Kraft (1983), has to be parallel to the NCL. In other words, its slope is also material constant λ owing to the assumption that the ratio of p_s to p_c is kept constant, i.e.,

$p_s/p_c = \zeta/(1+\zeta)$, in accordance with Eq. (5). Then, the following relationship is obtained:

$$\frac{p_c}{p_{c0}} = \frac{p_s}{p_{s0}} = \frac{F}{F_0} \tag{11}$$

where $F_0 (= p_{c0} - p_{s0})$ is the initial size of the yield locus. By substituting Eq. (11) into Eq. (9), the hardening law can be rewritten in terms of p_s or F as

$$\varepsilon_v^p = \frac{\lambda-\kappa}{1+e_{c0}} \ln \frac{p_s}{p_{s0}} = \frac{\lambda-\kappa}{1+e_{c0}} \ln \frac{F}{F_0}. \tag{12}$$

It should be noted that the denominator $(1+e_{c0})$ in Eq. (12) could be replaced by $(1+e_{s0})$ if e_{s0} is regarded as a reference void ratio from which the plastic volumetric strain starts to occur. However, there is no way of foreseeing whether the material will be subjected to loading or unloading, and thus, whether the first yielding occurs on the NCL or the PRL. In addition, there is not much difference between $(1+e_{c0})$ and $(1+e_{s0})$ in most cases, so that Eqs. (9) and (10) will be used in the analysis of this study as they are.

The yield condition of Eq. (7) can be rewritten in the quadratic equation for F, namely,

$$\zeta(1+\zeta)F^2 - (1+2\zeta)pF + p^2\left[1+\left(\frac{\eta}{\tilde{M}}\right)^2\right] = 0 \tag{13}$$

where η is a stress ratio defined by $\eta = q/p$. If $\zeta > 0$, the above equation has two real roots for the stress state of $\eta < \bar{M}$, whereas it has a double root only when $\eta = \bar{M}$, so that $r = 0$. In contrast, Eq. (13) yields a linear equation for variable F if the model corresponds to the modified Cam-clay model, i.e., $\zeta = 0$. Then,

$$F = \frac{\tilde{M}^2 + \eta^2}{\tilde{M}^2} p \quad \text{for } \zeta = 0 \tag{14}$$

and

$$F = \frac{1+2\zeta+\alpha r}{2\zeta(1+\zeta)} p; \quad r = r(\eta)$$
$$= \sqrt{1 - 4\zeta(1+\zeta)\left(\frac{\eta}{\tilde{M}}\right)^2} \quad \text{for } \zeta > 0 \tag{15}$$

where α becomes $+1$ or -1 corresponding to a region of the yield locus where the current stress is located at the contact point touching the limit line with slope $\bar{M}$ (see Fig. 1). It is obvious that function r in Eq. (15) becomes zero only when the current stress is located at that contact point, i.e., $\eta = \bar{M}$.

The summation of Eqs. (9) and (10), into which Eq. (14) or (15) is substituted, yields volumetric strain ε_v as a function of stress variables p and η. Moreover, if $\dot{\varepsilon}_v = 0$ is set, the explicit formulation of the effective stress path under the undrained condition can be obtained. Fig. 5(a) and (b) compare the effective stress paths from the initial states on the NCL ($p = p_{c0}$) and the PRL ($p = p_{s0}$) during undrained shear calculated using different values for the additional parameter, namely, $\zeta = 0.1$ and $\zeta = 1.0$, respectively. In order to identify only the effects of parameter ζ on the undrained shear behavior, the values for Λ and M are set to be common ($M = 1.0$ and $\Lambda = 0.75$), where Λ is the irreversibility defined as $\Lambda = (\lambda-\kappa)/\lambda$. As can be seen from these figures, the effective mean stress decreases with the expansion of the yield loci during the undrained shear from the state on the NCL, while it increases with the shrinkage of the yield loci even immediately after the start of undrained shear from the state on the PRL. It is also obvious that the larger value of additional parameter ζ contributes to suppressing changes in the effective mean stress due to the undrained shear up to the critical state. Such a shear response of the model complies with the interpretation of the dilatancy characteristic of saturated bentonite by Takayama et al. (2012).

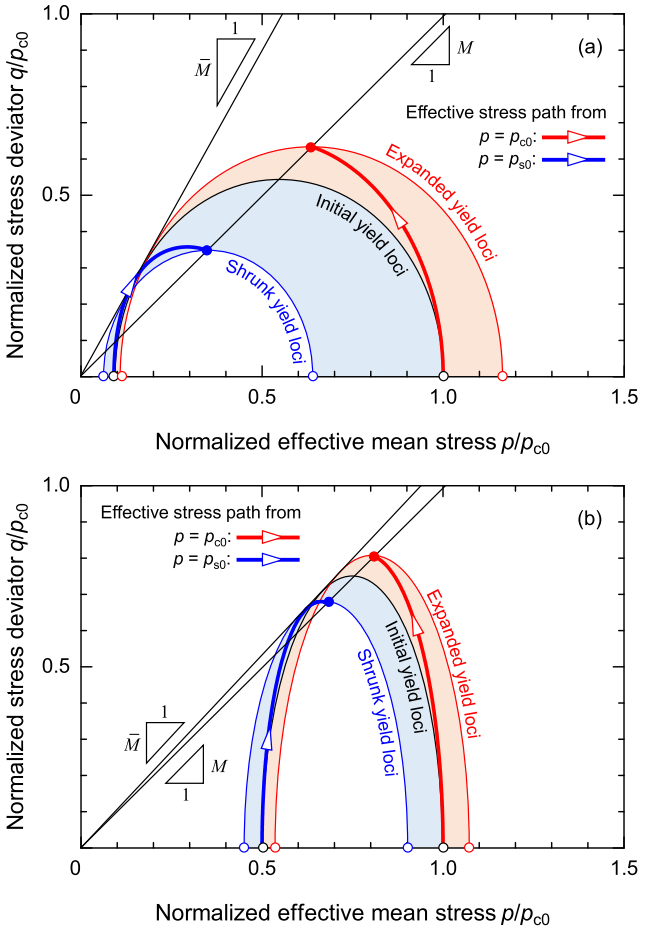

Fig. 5. Comparison of effective stress paths during undrained shear calculated with different values for additional parameter: (a) $\zeta = 0.1$ and (b) $\zeta = 1.0$.

For $\zeta > 0$ and $r \neq 0$, by taking the first time-differentiation of Eq. (12) after the substitution of Eq. (15), the plastic volumetric strain rate takes the following form:

$$\dot{\varepsilon}_v^p = \tilde{M} D \frac{\dot{F}}{F} = \tilde{M} D \left[\frac{\dot{p}}{p} - \alpha \frac{2\zeta(1+\zeta)}{1+2\zeta+\alpha r} \frac{2\eta}{r\tilde{M}^2} \dot{\eta}\right] \tag{16}$$

where $D=(\lambda-\kappa)/\left[\tilde{M}(1+e_{c0})\right]$ after the definition by Shibata (1963). The respective derivatives of f with p and q are

$$\frac{\partial f}{\partial p}=2p-(1+2\zeta)F=-\frac{1+\alpha(1+2\zeta)r}{2\zeta(1+\zeta)}p \tag{17}$$

$$\frac{\partial f}{\partial q}=2\frac{q}{\tilde{M}^2} \tag{18}$$

Then, if the associated flow rule is applied to describe the subsequent plastic deformation, the plastic shear strain rate yields

$$\begin{aligned}\dot{\varepsilon}_s^p&=\frac{\partial f/\partial q}{\partial f/\partial p}\dot{\varepsilon}_v^p\\&=-\tilde{M}D\frac{2\zeta(1+\zeta)}{1+\alpha(1+2\zeta)r}\frac{2\eta}{\tilde{M}^2}\left[\frac{\dot{p}}{p}-\alpha\frac{2\zeta(1+\zeta)}{1+2\zeta+\alpha r}\frac{2\eta}{r\tilde{M}^2}\dot{\eta}\right]\end{aligned} \tag{19}$$

On the other hand, the first time-differentiation of Eq. (10) results in the isotropic part of the elastic constitutive equation, as follows:

$$\dot{\varepsilon}_v^e=\frac{\kappa}{1+e_{c0}}\frac{\dot{p}}{p}=\tilde{M}D\frac{1-\Lambda}{\Lambda}\frac{\dot{p}}{p} \tag{20}$$

In addition, the elastic behavior is assumed to be isotropic, which leads to the development of shear strain with any changes in stress deviator q as

$$\dot{\varepsilon}_s^e=\frac{\tilde{M}D}{3\mu}\frac{1-\Lambda}{\Lambda}\frac{\dot{q}}{p};\quad \mu=\frac{3(1-2v)}{2(1+v)} \tag{21}$$

where v is a constant Poisson's ratio.

For the axisymmetric or triaxial condition, the rate of axial and radial strains can be described in terms of two invariants of the strain rate tensor, together with the additive decomposition of the strain rate into elastic and plastic parts, as the following pair of equations:

$$\dot{\varepsilon}_a=\frac{1}{3}\dot{\varepsilon}_v+\dot{\varepsilon}_s=\frac{1}{3}\left(\dot{\varepsilon}_v^e+\dot{\varepsilon}_v^p\right)+\left(\dot{\varepsilon}_s^e+\dot{\varepsilon}_s^p\right) \tag{22}$$

$$\dot{\varepsilon}_r=\frac{1}{3}\dot{\varepsilon}_v-\frac{1}{2}\dot{\varepsilon}_s=\frac{1}{3}\left(\dot{\varepsilon}_v^e+\dot{\varepsilon}_v^p\right)-\frac{1}{2}\left(\dot{\varepsilon}_s^e+\dot{\varepsilon}_s^p\right). \tag{23}$$

Then, by substituting Eqs. (16), (19), (20) and (21) into these equations, with the relation $\dot{q}/p=\dot{\eta}+\eta(\dot{p}/p)$, the rate form of the constitutive relation at the elasto-plastic state in the matrix form can be summarized as

$$\begin{Bmatrix}\dot{\varepsilon}_a\\ \dot{\varepsilon}_r\end{Bmatrix}=\tilde{M}D\begin{bmatrix}C_{11}&C_{12}\\C_{21}&C_{22}\end{bmatrix}\begin{Bmatrix}\dot{p}/p\\ \dot{\eta}\end{Bmatrix} \tag{24}$$

Individually,

$$C_{11}=\frac{1}{3\Lambda}+\frac{1-\Lambda}{3\mu\Lambda}\eta-\frac{2\zeta(1+\zeta)}{1+\alpha(1+2\zeta)r}\frac{2\eta}{\tilde{M}^2} \tag{25}$$

$$C_{12}=\frac{1-\Lambda}{3\mu\Lambda}-\alpha\left(\frac{1}{3}-\frac{2\zeta(1+\zeta)}{1+\alpha(1+2\zeta)r}\frac{2\eta}{\tilde{M}^2}\right)\frac{2\zeta(1+\zeta)}{1+\alpha(1+2\zeta)r}\frac{2\eta}{r\tilde{M}^2} \tag{26}$$

$$C_{21}=\frac{1}{3\Lambda}-\frac{1}{2}\frac{1-\Lambda}{3\mu\Lambda}\eta+\frac{1}{2}\frac{2\zeta(1+\zeta)}{1+\alpha(1+2\zeta)r}\frac{2\eta}{\tilde{M}^2} \tag{27}$$

$$C_{22}=-\frac{1}{2}\frac{1-\Lambda}{3\mu\Lambda}-\alpha\left(\frac{1}{3}+\frac{1}{2}\frac{2\zeta(1+\zeta)}{1+\alpha(1+2\zeta)r}\frac{2\eta}{\tilde{M}^2}\right)\frac{2\zeta(1+\zeta)}{1+\alpha(1+2\zeta)r}\frac{2\eta}{r\tilde{M}^2}. \tag{28}$$

The relation between the principal components of stress and strain in the rate form can be obtained by substituting the following equation into Eq. (24):

$$\begin{Bmatrix}\dot{p}/p\\ \dot{\eta}\end{Bmatrix}=\frac{1}{3p}\begin{bmatrix}1&2\\3-\eta&-3-2\eta\end{bmatrix}\begin{Bmatrix}\dot{\sigma}_a\\ \dot{\sigma}_r\end{Bmatrix} \tag{29}$$

in which $\dot{\sigma}_a$ and $\dot{\sigma}_r$ are the rate of the axial and radial effective stresses, respectively, satisfying the relations $p=(\sigma_a+2\sigma_r)/3$ and $q*=\sigma_a-\sigma_r$ where $q*$ is the difference in stress.

This section formulated the model in terms of invariants or triaxial components of stress and strain to clarify the connection to the analyses in the latter one. Meanwhile, the model can be expanded to the general tensorial form on the hypothesis of isotropy, as described in the Appendix, so that it will function in the multi-dimensional finite element analysis. In what follows, the explicit method will be used to numerically solve the nonlinear system of constitutive equations with a possible small-size stress or strain increment to avoid the accumulation of numerical errors.

3. Analytical investigation of consolidation and swelling

Both consolidation and swelling in axial and radial problems shall be analytically addressed in order to obtain some insight into the applicability and limitations of the constitutive model with or without the concept of plastic rebound. Herein, the axial problem indicates the volume change behaviours under the condition of no radial deformation ($\dot{\varepsilon}_r=0$) commonly observed in an oedometer test, while the radial problem indicates the volume change behaviours under the condition of no axial deformation ($\dot{\varepsilon}_a=0$) possibly achieved in the axisymmetric triaxial system. Although very few experimental investigations have been made on radial problems compared to axial ones, probably due to the difficulty involved with performing them, whether the state of the material is saturated or unsaturated, it is essential to understand how the constitutive model predicts the behaviours ahead of its application to boundary value problems.

3.1. Comparison of predicted consolidation and swelling paths

Through a series of calculations of consolidation and swelling in the axial and radial problems, we shall examine how the concept of plastic rebound serves to predict these

behaviours. A common set of material inputs is used for all the calculations in this section: $\tilde{M} = 1.0$, $\Lambda = 0.8$ and $\nu = 0.333$, except for parameter ζ.

Figs. 6 and 7 show the numerical results for consolidation and swelling in the axial and radial problems, respectively: (a) effective stress paths and (b) changes in stress ratio with axial strain ε_a for the axial problem and radial strain ε_r for the radial one. Herein, the value for ζ is set to be zero in order to obtain the results equivalent to those by a modified Cam-clay model. Each stress path has a starting point on the initial yield locus and traces either a consolidation or a swelling path to maintain the elasto-plastic state. Since the effective stress path within an elastic domain in the p-q space has an elastic gradient of $\dot{q}/\dot{p} = 2\mu$ for the axial deformation and $\dot{q}/\dot{p} = -\mu$ for the radial one, two points having a tangent with each elastic gradient separate a closed initial yield locus into two domains, namely, the surface where the loading brings about the plastic deformation and the surface where the unloading brings about the plastic deformation.

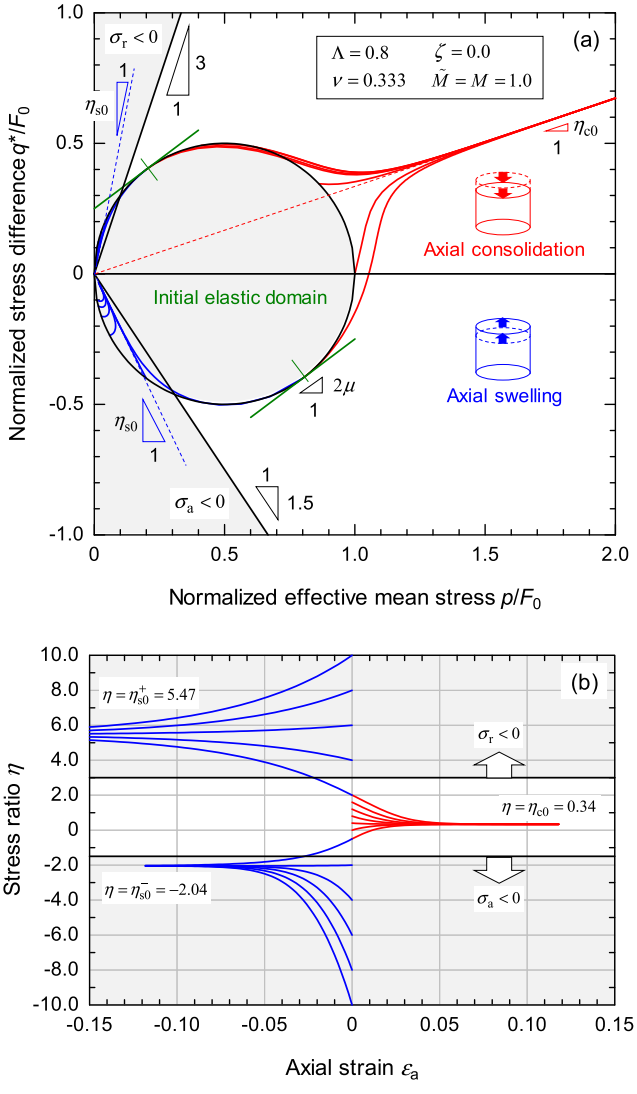

Fig. 6. Numerical results for consolidation and swelling in axial problem with $\zeta = 0.0$: (a) effective stress paths and (b) changes in stress ratio with axial strain ε_a.

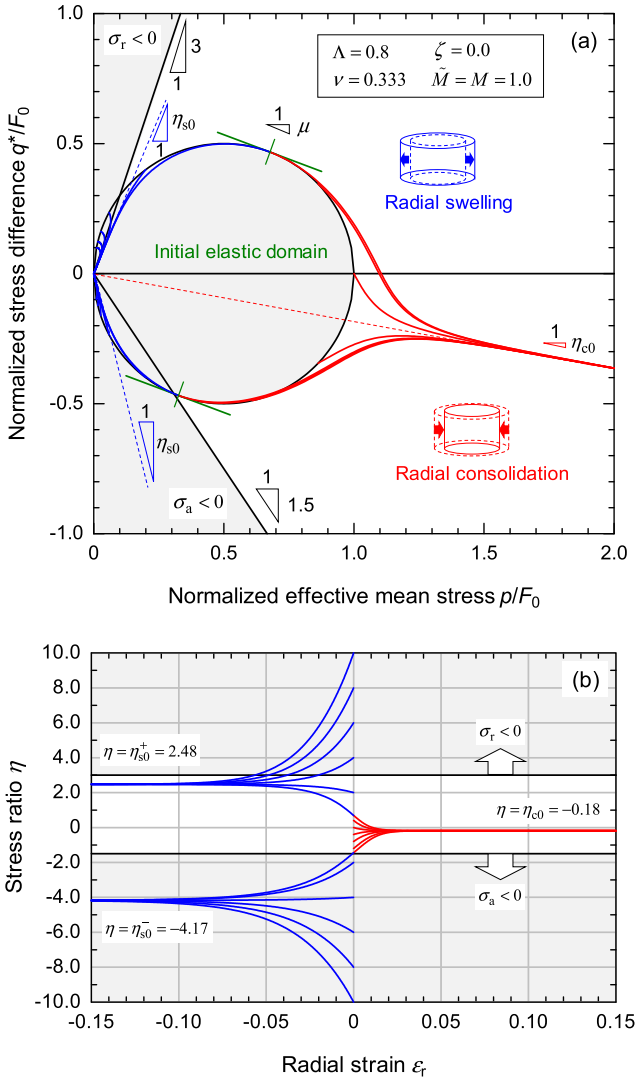

Fig. 7. Numerical results for consolidation and swelling in radial problem with $\zeta = 0.0$: (a) effective stress paths and (b) changes in stress ratio with radial strain ε_r.

As can be seen from the figures, each of the axial and radial consolidation paths converges toward a unique dashed straight line, i.e., K_0-consolidation line, with a slope denoted by η_{c0} whose value is 0.34 for the axial consolidation and −0.18 for the radial one. Meanwhile, as for swelling responses, patterns for the elasto-plastic effective stress path can be unexpectedly demarcated into two types. One is the path from the starting point in a negative region of stress difference ($q* = \sigma_a - \sigma_r < 0$) which converges toward the line leading to the origin, while keeping the stress difference negative. The other is the path from the starting point in a positive region of stress difference ($q* > 0$) which approaches the origin, while keeping the stress difference positive. In so far as the axial swelling is concerned, the former appears to include the prediction of the effective stress path common in the unloading process of the oedometer

test. However, it is likely that the latter is an unrealistic prediction when considering the experimental fact that the coefficient of earth pressure at rest typically exceeds 1.0 in the process of axial swelling up to a heavily overconsolidated state. Similarly, it would be plausible, at least intuitively, for the radial swelling paths to also have unique, but positive, convergence stress ratios compared to that predicted for the radial consolidation. However, as Fig. 7 indicates, the model predicts two convergence stress ratios in positive and negative regions of stress difference.

As a matter of fact, it may not be worth the inconvenience when one considers either axial or radial problems because the yielding of the material upon unloading after the elasto-plastic consolidated state is always predicted to occur in either a positive or negative region of the stress difference in accordance with the problem. However, in more complicated, but general, cases, where radial swelling occurs followed by axial swelling, or vice versa, the problem will surface because the positive/negative stress difference determined at the initial yielding upon swelling never becomes opposite in the steps of the swelling process. In other words, a magnitude relationship between axial and radial effective stresses cannot be replaced even though there is a change in the direction of swelling. Incidentally, it should be pointed out that the effective stress paths upon swelling, shown in Figs. 6 and 7, easily enter either region where the effective axial or radial stress is negative, which implies that the set of input parameters used in these calculations limits the swelling deformation achieved under a positive stress condition.

Examples of similar calculations to those mentioned above, but with the different value of $\zeta = 0.5$, are shown in Figs. 8 and 9. In contrast to the cases with $\zeta = 0.0$, the yield locus is separated from the origin of the effective stress space by setting a non-zero value for ζ, which allows the prediction of a specific convergence stress ratio for each consolidation and swelling in both axial and radial problems. Also of interest is its ability to obtain the effective stress path which traverses the p-axis in the process of elasto-plastic swelling.

3.2. Conditions for predicting realistic convergence stress ratios

It has become obvious that parameter ζ, being non-zero, has an effect on the patterns of the effective stress path, especially in the process of elasto-plastic swelling through the comparison in the preceding section. Thus, this section explores the conditions imposed on the determination of input parameters to predict one convergence stress ratio for each consolidation and swelling in the axial and radial problems after examining the characteristics of the constitutive model.

Let us first consider the convergence condition of $\dot{\eta} = 0$ for the axial problem. By imposing the radial constraint condition of $\dot{\varepsilon}_r = 0$, Eqs. (24) and (29) provide the following relations:

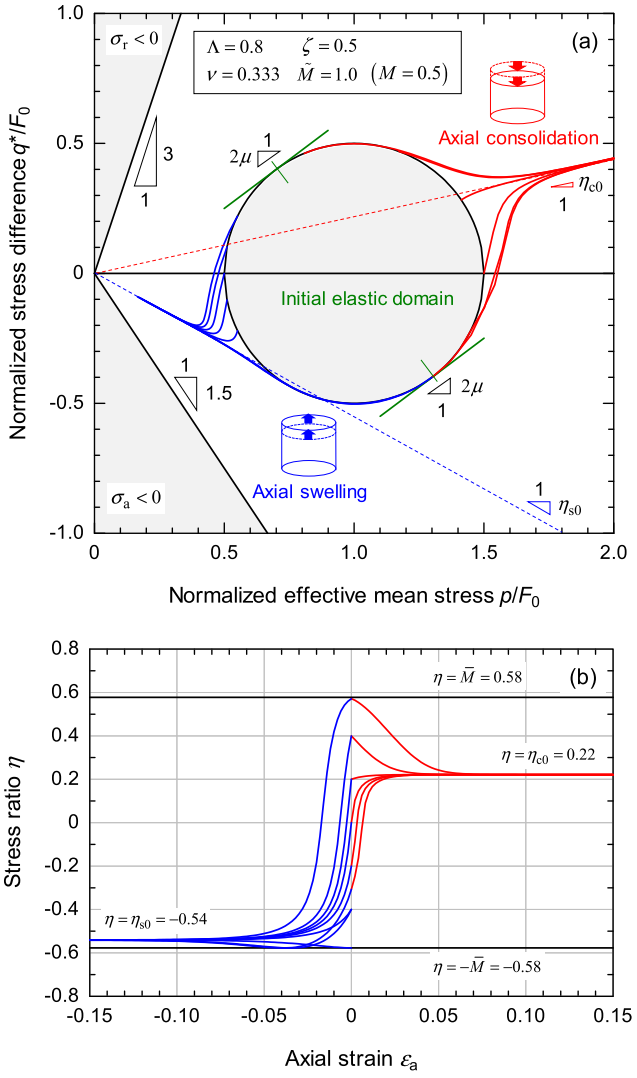

Fig. 8. Numerical results for consolidation and swelling in axial problem with $\zeta = 0.5$: (a) effective stress paths and (b) changes in stress ratio with axial strain ε_a.

$$\dot{\sigma}_r = -\frac{C_{21} + (3-\eta)C_{22}}{2C_{21} - (3+2\eta)C_{22}}\dot{\sigma}_a \tag{30}$$

$$\dot{p} = -\frac{3C_{22}}{2C_{21} - (3+2\eta)C_{22}}\dot{\sigma}_a \tag{31}$$

$$\dot{\eta} = \frac{3C_{21}}{2C_{21} - (3+2\eta)C_{22}}\frac{1}{p}\dot{\sigma}_a \tag{32}$$

Thus, from Eq. (32), it follows that the convergence condition in the axial problem can be satisfied by $C_{21} = 0$ for any given axial effective stress rate $\dot{\sigma}_a$. At that time, Eq. (30) yields

$$\dot{\sigma}_r = \frac{3-\eta_0}{3+2\eta_0}\dot{\sigma}_a \equiv K_0\dot{\sigma}_a \tag{33}$$

where η_0 is the stress ratio which satisfies $\dot{\eta} = 0$ and K_0 is a so-called coefficient of earth pressure at rest.

On the other hand, for the radial problem, by imposing the axial constraint condition of $\dot{\varepsilon}_a = 0$, Eqs. (24) and (29) yield

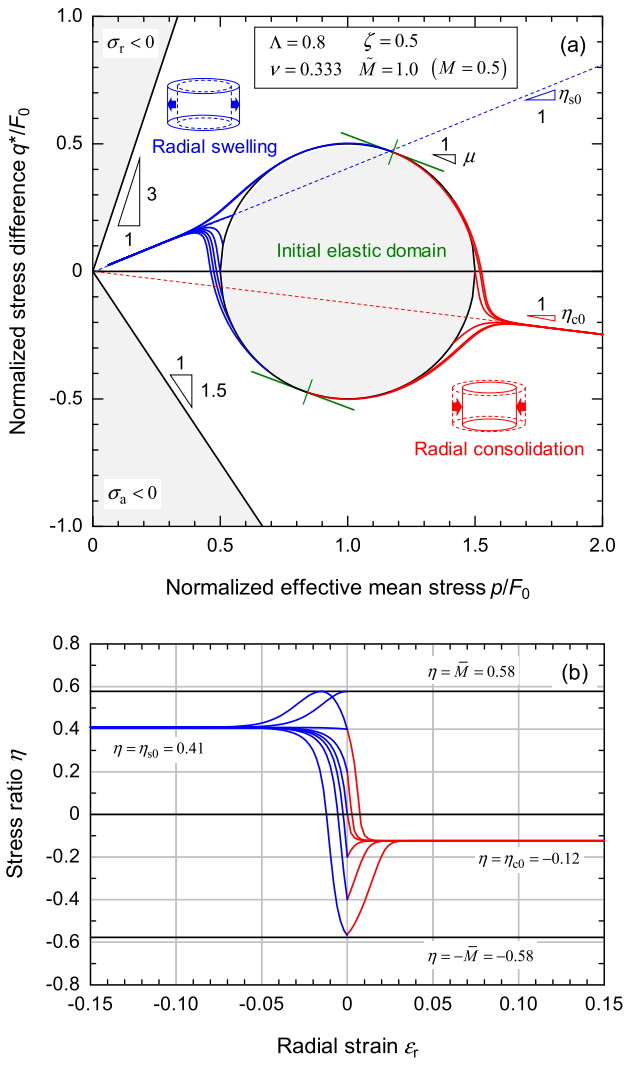

Fig. 9. Numerical results for consolidation and swelling in radial problem with $\zeta = 0.5$: (a) effective stress paths and (b) changes in stress ratio with radial strain ε_r.

$$\dot{\sigma}_a = -\frac{2C_{11} - (3+2\eta)C_{12}}{C_{11} + (3-\eta)C_{12}}\dot{\sigma}_r \tag{34}$$

$$\dot{p} = \frac{3C_{12}}{C_{11} + (3-\eta)C_{12}}\dot{\sigma}_r \tag{35}$$

$$\dot{\eta} = \frac{3C_{11}}{C_1 + (3-\eta)C_{12}}\frac{1}{p}\dot{\sigma}_r \tag{36}$$

Then, from Eq. (36), it turns out that the convergence condition in the radial problem can be satisfied by $C_{11} = 0$ for any given radial effective stress increment $\dot{\sigma}_r$. When $C_{11} = 0$, Eq. (34) yields the relationship between the axial and radial effective stress rates with exactly the same formulation as Eq. (33).

Since it is difficult to solve the convergence conditions of $C_{21} = 0$ and $C_{11} = 0$ for stress ratio η explicitly, the variations in C_{21} and C_{11} will be examined within the possible range of stress ratios in order to estimate the number of solutions. Although these functions are formulated as indicated in Eqs. (25) and (27), they can lead to the extra formation in cases where $\zeta = 0.0$ as

$$C_{11} = \frac{1}{3\Lambda} + \frac{1-\Lambda}{3\mu\Lambda}\eta + \frac{2\eta}{M^2 - \eta^2} \tag{37}$$

$$C_{21} = \frac{1}{3\Lambda} - \frac{1}{2}\frac{1-\Lambda}{3\mu\Lambda}\eta - \frac{\eta}{M^2 - \eta^2} \tag{38}$$

It should be noted that, when C_{21} is zero in Eq. (38), the equation can be rearranged to yield the condition for η_0 appearing in Wood (1990), although the symbol η_{Knc} was used instead of η_0 in his book.

Fig. 10(a)–(d) show the variations in C_{21} with stress ratio η normalized by its maximum $\bar{M}$ for ζ values of 0.0, 0.005, 0.05 and 0.5, respectively, together with a common set of inputs, namely, $\tilde{M} = 1.0$, $\Lambda = 0.8$ and $\nu = 0.333$. Herein, the value for $\bar{M}$ is set to be 10.0 only in Fig. 10(a), for the sake of convenience, since it becomes infinite when $\zeta = 0.0$ according to the definition in Eq. (6). The shaded areas in the figures indicate the regions where the axial or radial effective stress is negative.

As shown in Fig. 10(a), for $\zeta = 0.0$, function C_{21} has two asymptotes: one at $\eta = -M$ and the other at $\eta = M$. It is found that there are three solutions which can satisfy $C_{21} = 0$; they are symbolized by triangles for consolidation and inverse triangles for swelling, being located in each of the regions: $\eta < -M$, $-M < \eta < M$ and $\eta > M$. It would be plausible to interpret the solutions in $-M < \eta < M$ and $\eta < -M$ as the proper predictions for the convergence stress ratios for axial consolidation and swelling, respectively, while it is difficult to give a physical meaning to the solution in $\eta > M$. On the other hand, in the case where $\zeta > 0.0$, two values for C_{21} can be determined for stress ratio η, except for $\eta = \pm\bar{M}$, owing to the characteristics of Eq. (13), as drawn by solid and broken lines in Fig. 10 (b)–(d). The broken line shares the same values at $\eta = -\bar{M}$ and $\eta = +\bar{M}$ as the solid one, and it is continuously distributed within the limits. As for a considerably lower value for ζ, with which the yield locus almost touches the origin of the effective stress space, there is an additional solution, which brings the number of solutions to four, as shown in Fig. 10(b), probably because the value for C_{21} at $\eta = +\bar{M}$ is negative. Actually, as can be seen in Fig. 10(c) and (d), with larger values for ζ, if only the value for C_{21} at $\eta = +\bar{M}$ is positive, the number of solutions decreases to two: one for consolidation and the other for swelling, whether the value at $\eta = -\bar{M}$ is positive or negative.

In a similar way, the variations in C_{11}, with stress ratio η normalized by its maximum $\bar{M}$, are shown in Fig. 11 in order to examine the number of converging stress ratios in the radial consolidation and swelling. As seen in Fig. 11(a), for $\zeta = 0.0$, function C_{11} also has two asymptotes at $\eta = -M$ and $\eta = M$. It is formed in a vertically

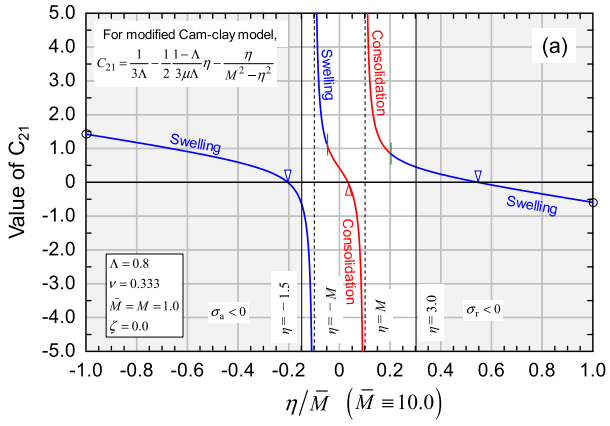

(a) Variations in C_{21} with possible range in stress ratio η when $\zeta = 0.0$

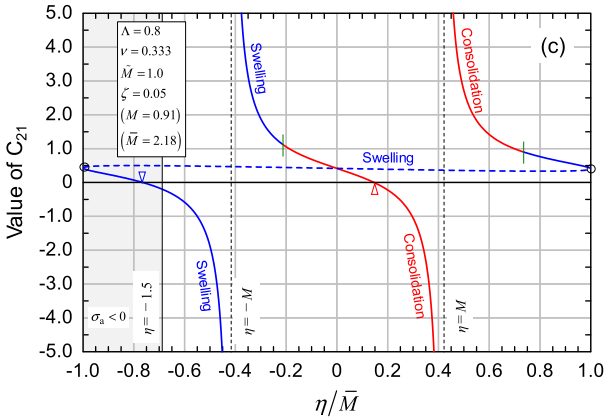

(c) Variations in C_{21} with possible range in stress ratio η when $\zeta = 0.05$

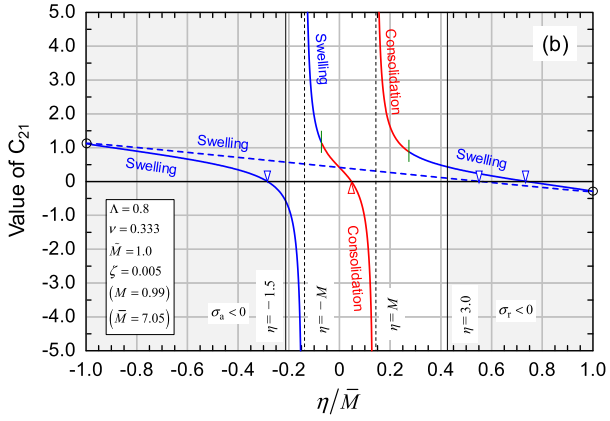

(b) Variations in C_{21} with possible range in stress ratio η when $\zeta = 0.005$

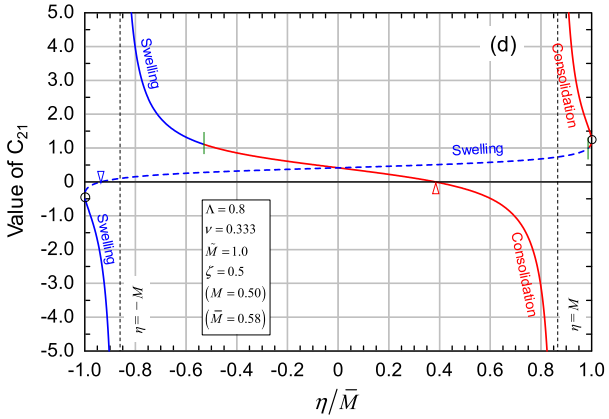

(d) Variations in C_{21} with possible range in stress ratio η when $\zeta = 0.5$

Fig. 10. Variations in C_{21} with possible range in stress ratio η.

symmetric shape with function C_{21} in Fig. 10(a). Once again, when $\zeta = 0.0$, the results show that there are three solutions in each of the regions: $\eta < -M$, $-M < \eta < M$ and $\eta > M$. When ζ is not zero, the variation in C_{11} indicated by a broken line is distributed in addition to the one indicated by a solid line. It is found from Fig. 11(b)–(d) that the number of solutions depends on the distribution of these two lines, and that it is actually determined by the sign of C_{11} at $\eta = -\bar{M}$.

Hence, judging from the above results, it can be argued that the values for C_{21} at $\eta = +\bar{M}$ and C_{11} at $\eta = -\bar{M}$, being positive, are crucial for determining the number of convergence stress ratios in axial and radial problems, respectively. In the axial problem, the necessary condition for the set of input parameters to allow the number of convergence stress ratios to be two can be satisfied when $C_{21} > 0$ at $\eta = +\bar{M}$. Thus, after substituting $\eta = +\bar{M}$ with Eqs. (4) and (6), and $r = 0$ into Eq. (27), the following equation can be obtained:

$$C_{21}|_{\eta=M^-} = \frac{1}{3\Lambda} - \frac{1}{2}\frac{1-\Lambda}{3\mu\Lambda}\bar{M} + \frac{1}{2}\frac{1}{\bar{M}} > 0 \tag{39}$$

from which a set of input parameters needs to fulfill the following inequality:

$$\frac{\mu}{1-\Lambda} + \sqrt{\frac{\mu}{1-\Lambda}\left(\frac{\mu}{1-\Lambda} + 3\Lambda\right)} > \frac{1+2\zeta}{2\sqrt{\zeta(1+\zeta)}}M\left(= \bar{M} > 0\right) \tag{40}$$

where the right-hand side is determined by critical state parameter M and parameter ζ, while the left-hand side is determined by irreversibility Λ and Poisson's ratio ν via $\mu = \{3(1-2\nu)\}/\{2(1+\nu)\}$. On the other hand, in the radial problem, since the necessary condition for obtaining two convergence stress ratios can be satisfied when $C_{11} > 0$ at $\eta = -\bar{M}$, after substituting $\eta = +\bar{M}$ with Eqs. (4) and (6), and $r = 0$ into Eq. (25), the following equation can be obtained:

$$C_{11}|_{\eta=-M^-} = \frac{1}{3\Lambda} - \frac{1-\Lambda}{3\mu\Lambda}\bar{M} + \frac{1}{\bar{M}} > 0 \tag{41}$$

from which a set of input parameters is needed to fulfill the following inequality:

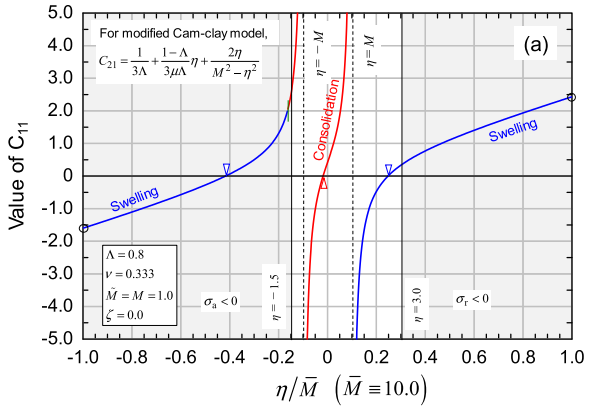

(a) Variations in C_{11} with possible range in stress ratio η when $\zeta = 0.0$

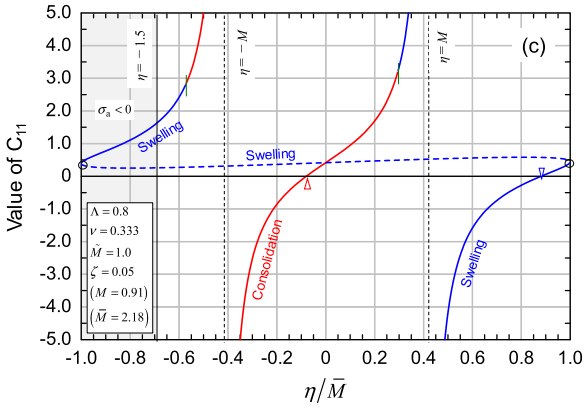

(c) Variations in C_{11} with possible range in stress ratio η when $\zeta = 0.05$

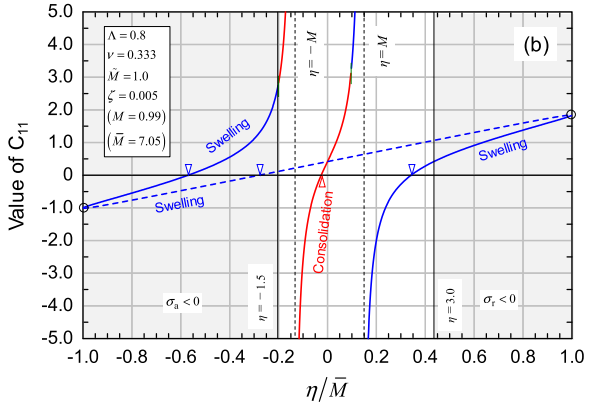

(b) Variations in C_{11} with possible range in stress ratio η when $\zeta = 0.005$

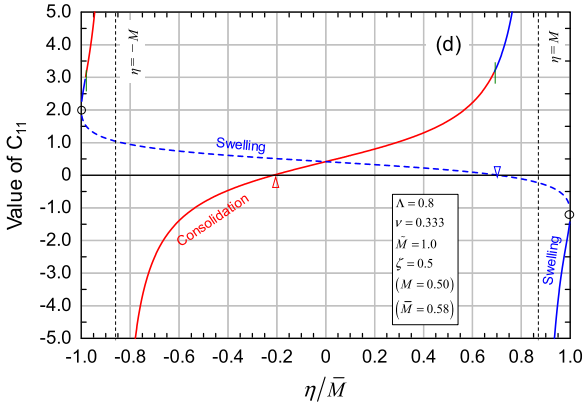

(d) Variations in C_{11} with possible range in stress ratio η when $\zeta = 0.5$

Fig. 11. Variations in C_{11} with possible range in stress ratio η.

$$\frac{1}{2}\frac{\mu}{1-\Lambda}+\sqrt{\frac{1}{2}\frac{\mu}{1-\Lambda}\left(\frac{1}{2}\frac{\mu}{1-\Lambda}+6\Lambda\right)} > \frac{1+2\zeta}{2\sqrt{\zeta(1+\zeta)}}M\left(=\bar{M}>0\right) \tag{42}$$

Fig. 12 presents a diagram for discriminating whether the inequalities of Eqs. (40) and (42) hold or not against the combination of four parameters. Herein, the variations on the right-hand side, depending on M and ζ, are represented by solid lines, while those on the left-hand side of Eqs. (40) and (42), depending on ν and Λ, are represented by broken lines with painted and outlined marks, respectively. In order to obtain one convergence stress ratio for each consolidation and swelling, a set of parameters should be determined so that the value on the right-hand side is smaller than that on the left-hand side. As the diagram indicates, the right-hand side of inequalities monotonically decreases with an increase in ζ, while the left-hand side in both Eqs. (40) and (42) monotonically increases with an increase in irreversibility Λ. Therefore, the smaller the value of ζ, the more easily the inequalities are violated.

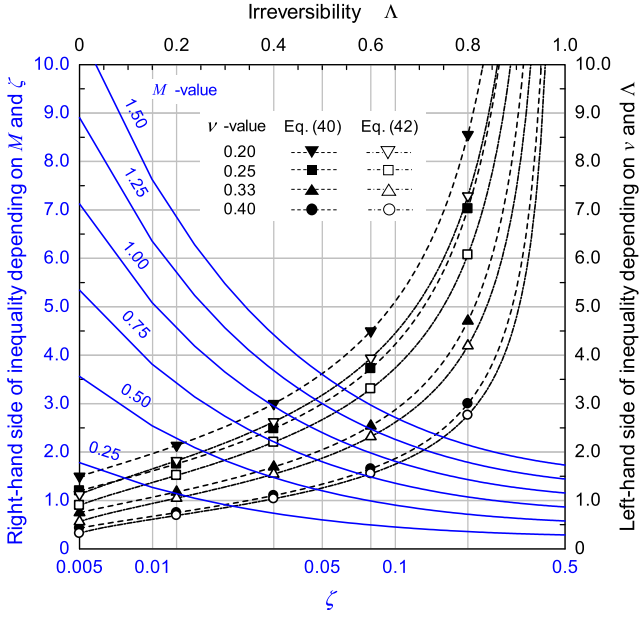

Fig. 12. Diagram for discriminating whether inequalities of Eqs. (40) and (42) hold or not against combination of four parameters: M, ζ, Λ and ν.

Since $\bar{M}$ is positive infinite when $\zeta = 0.0$, an application of the yield locus passing the origin of the effective stress space always violates both inequalities.

3.3. Analytical estimation of K_0 values

A pair of values for convergence stress ratio η_0 can be obtained by numerically solving $C_{21} = 0$ for the axial problem and $C_{11} = 0$ for the radial one using the bisection method against a set of material inputs of Λ, ν, ζ and M which satisfies the inequalities in the preceding section. In what follows, for less confusion, the convergence stress ratio for consolidation will be denoted by η_{c0}, while that for swelling will be denoted by η_{s0}. Furthermore, the corresponding coefficients of earth pressure at rest, K_{c0} and K_{s0}, are formulated in a similar style to Eq. (33), respectively, as

$$K_{c0} = \frac{3 - \eta_{c0}}{3 + 2\eta_{c0}} \text{ and } K_{s0} = \frac{3 - \eta_{s0}}{3 + 2\eta_{s0}} \tag{43}$$

Figs. 13 and 14 show the variations in (a) K_{c0} and (b) K_{s0} for the axial problem in relation to effective friction angle ϕ being linked with M through $\sin\phi = 3M/(6 + M)$. The value of irreversibility Λ is set to be 0.8 and 0.4 in Figs. 13 and 14, respectively. The variations in K_{c0} are represented by solid lines in cases where the corresponding value for K_{s0} is estimated as positive or $\eta_{s0} > -3/2$, whereas they are represented by broken lines in cases where the corresponding value for K_{c0} is $K_{s0} < 0$ ($\eta_{s0} < -3/2$). However, negative values for K_{s0} are not represented in Figs. 13(b) or 14(b). It is found from these figures that larger values for ζ yield larger reductions in K_{c0} with an increase in ϕ, while smaller values for ζ are apt to lead to larger K_{c0} than those calculated with Jaky's empirical formula (Jaky, 1944; Jaky, 1948). In addition, larger values for ζ allow the values for K_{s0} to be positive over a wider range of ϕ, while smaller values yield positive K_{s0} only in the range where the values for ϕ are relatively smaller. This suggests that it is necessary to pay attention when determining a set of material parameters particularly in the prediction of simultaneous changes in axial and radial effective stresses due to swelling.

The variations in (a) K_{c0} and (b) K_{s0} for the radial problem, in relation to effective friction angle ϕ, are also shown in Fig. 15 with $\Lambda = 0.8$ and in Fig. 16 with $\Lambda = 0.4$. By comparison, it turns out that the variation in K_{c0} becomes more sensitive to the value of Poisson's ratio ν when Λ is smaller, although the values for ζ are more dominant when Λ is larger, which could also be seen in the axial consolidation. Although few attempts have been made at an experimental investigation into the radial swelling of expansive soils, Dueck et al. (2016) reported the measurement results for the evolutions of axial and radial stresses together with the applied water pressure on a radially swelled and saturated Wyoming bentonite (MX-80) specimen. According to those results, the value for K_{s0} is estimated to be from approximately 0.7 to 0.8. On the other hand, the effective friction angle of MX-80 can be estimated to be about 10 degrees, which corresponds to $M = 0.37$, according to the results of undrained shear tests conducted by Börgesson et al. (1995) and Dueck et al. (2010). In summation, the predicted values for K_{s0} between $\zeta = 0.5$ and 1.0, shown in Figs. 15 and 16, are satisfactorily consistent with the experimental results.

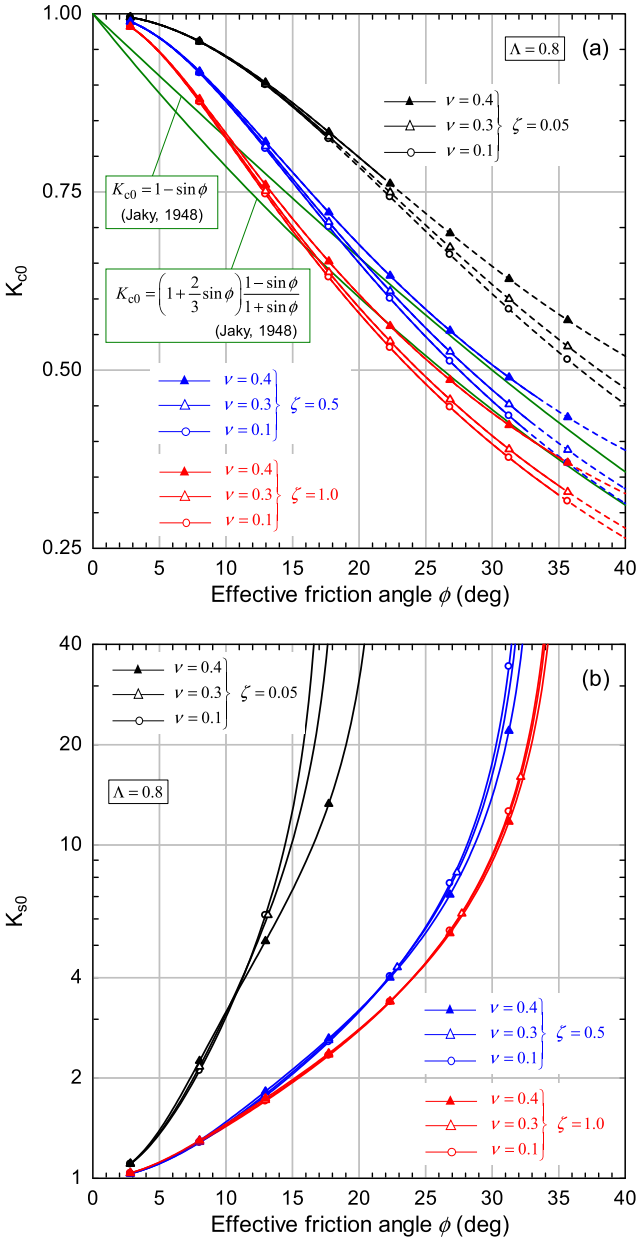

Fig. 13. Variations in coefficient of earth pressure at rest: (a) K_{c0} for consolidation and (b) K_{s0} for swelling in axial problem with $\Lambda = 0.8$.

4. Results of simulation

This section compares the results of a simulation with those of laboratory tests on expansive soils in order to validate the capabilities of the constitutive model with the plastic rebound concept. The laboratory tests consisted of

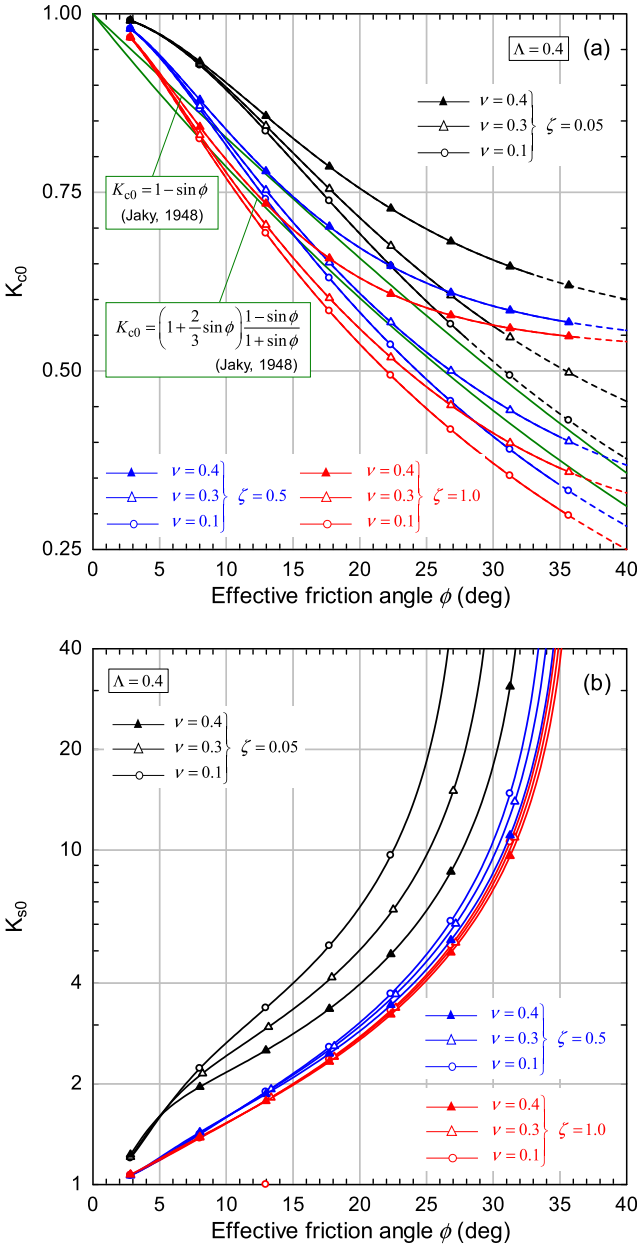

Fig. 14. Variations in coefficient of earth pressure at rest: (a) K_{c0} for consolidation and (b) K_{s0} for swelling in axial problem with $\Lambda = 0.4$.

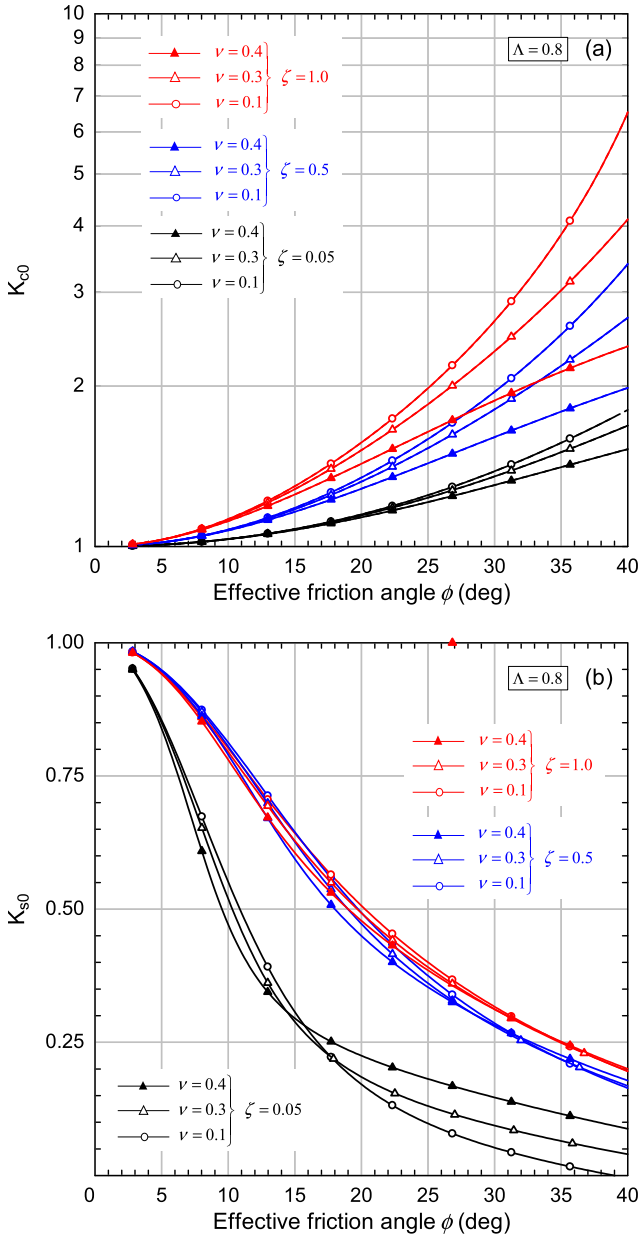

Fig. 15. Variations in coefficient of earth pressure at rest: (a) K_{c0} for consolidation and (b) K_{s0} for swelling in radial problem with $\Lambda = 0.8$.

odometer and undrained shear tests on saturated sodium-type bentonite (Namikawa and Sugano, 1997a, 1997b) and on a saturated mixture of sodium-type bentonite and sand (Takaji and Suzuki, 1999).

4.1. Simulations of laboratory tests on the saturated sodium-type bentonite

The oedometer test on the saturated sodium-type bentonite (Kunigel V1), which was conducted by Namikawa and Sugano (1997a), comprised three processes: loading, unloading and reloading. In the preparatory stage, the bentonite sample was compacted at a water content of 5.7% to a prescribed dry density of 1.6 Mg/m^3; then it was subjected to the supplement of distilled water up to its saturation, while the volume was kept constant in a similar way to that of the swelling pressure test. The test proceeded to the loading process without the release of the swelling pressure that had been generated in the saturation process. The sample was stepwisely consolidated up to the maximum overburden or axial stress of 19.8 MPa; then it was subjected to stepwise unloading toward an overburden of 0.64 MPa, that almost corresponded to the swelling pressure, followed by stepwise reloading toward 19.8 MPa. During testing, the axial displacement or volume change of the specimen was continuously measured, but the radial

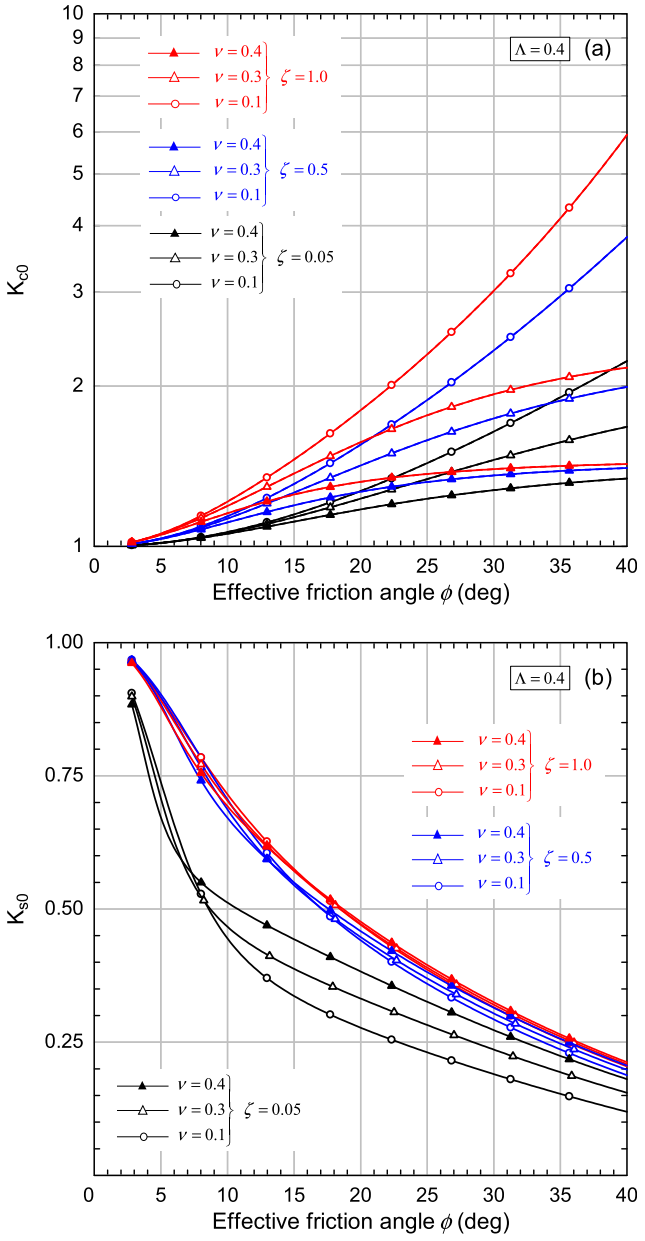

Fig. 16. Variations in coefficient of earth pressure at rest: (a) K_{c0} for consolidation and (b) K_{s0} for swelling in radial problem with $\Lambda = 0.4$.

stress was not. Although three tests were conducted under the same conditions, there appeared to be few differences among the results, i.e., changes in void ratio.

On the other hand, five triaxial compression tests reported in Namikawa and Sugano (1997b) were conducted on saturated sodium-type bentonite samples under the undrained condition, but with different confining pressures. The samples were compacted at water contents of 9.3–12.0% to the prescribed dry density of 1.6 Mg/m^3 and had a diameter of 50 mm and a height of 100 mm; then they were subjected to the supplement of distilled water in the saturation cells for several months. Saturated and dismantled samples were set in the triaxial apparatus and isotropically consolidated up to each prescribed consolidation pressure. After measuring the B-value, the samples were monotonically sheared under the undrained condition at a constant axial strain rate of 0.01 mm/min.

Table 1 shows the parameters adopted for the simulation. Critical state parameter M was determined from the residual stress states obtained from a series of undrained shear tests. Compression index λ was estimated based on both the $e - \ln\sigma$ relation in the loading process for the oedometer test and the line through the points on the $e - \ln p$ plane representing the isotropically consolidated stress states of undrained shear tests. The initial slope of the $e - \ln\sigma$ relation in the unloading process of the oedometer test was basically used for determining elastic swelling index κ. The other parameters were then calibrated from the results of the oedomoter test including the unloading process and undrained shear tests.

Fig. 17 shows the simulated and experimental results of the oedometer test, i.e., the $e - \ln\sigma$ relation. The initial stress state was assumed to be isotropic in the simulation since it was impossible to specify the initial value of the radial effective stress. As seen in the figure, the large swelling upon unloading appears to be favorably simulated by the constitutive model with a plastic rebound concept. It

Table 1
Model parameters for sodium-type bentonite (Kunigel V1).

λ	Compression index	0.12*
Λ	Irreversibility	0.58*
M	Critical state parameter	0.58**
ζ	Plastic rebound parameter	0.45**
ν	Poisson's ratio	0.21
e_{ref}	Reference combination on NCL	0.70
p_{ref} (MPa)		1.50

* Corresponding value of elastic swelling index: $\kappa = (1 - \Lambda)\lambda = 0.0504$.
** Corresponding value of ellipticity: $M = (1 + 2\zeta)M = 1.102$.

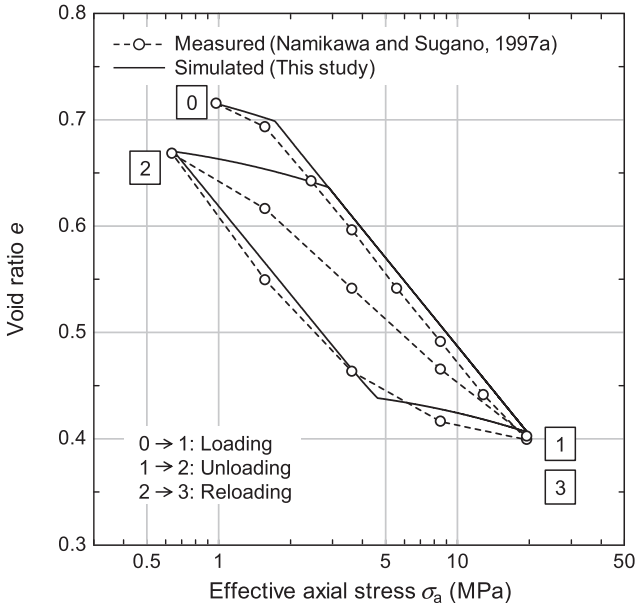

Fig. 17. Comparison of simulated and experimental results of oedometer test on sodium-type bentonite (Namikawa and Sugano, 1997a).

does not seem to be altogether amiss to assume the existence of the plastic rebound line in the $e - \ln p$ plane with the same slope as the normal consolidation line. On the other hand, it is found that problems still remain in the prediction capability for the reloading path. In other words, the model should provide results such that the compressibility from quite an early stage of reloading becomes larger. This disadvantage will be resolved if one considers the subloading surface concept (Hashiguchi, 1980; Hashiguchi, 1989), which enables the description of a smooth elastic-plastic transition and the development of plastic strain, even when the current stress is located in the interior of the ordinary yield locus.

The initial conditions for the simulation of the undrained shear tests are summarized in Table 2 and are plotted in Fig. 18 together with the NCL and the PRL determined by the set of input parameters in Table 1. The simulated results of the initial loading process of the oedometer test are also drawn by a dashed line in the figure for comparison. Among the five test cases, the initial state of only CU1-1 was regarded as overconsolidated, since the combination of initial effective mean stress and void ratio provided in the report by Namikawa and Sugano (1997b) was clearly located between the assumed NCL and PRL. Thus, the reported initial values were used in the simulation as they were, from which the value of the overconsolidation ratio was calculated as 1.45. On the other hand, the initial states of the other four cases from CU1-2 to CU1-5 were set to be normally consolidated because they were almost located on the assumed NCL. However, the reported values of the initial void ratio in the parentheses in Table 2 were modified in the simulation so as to satisfy each yield condition keeping the effective mean stress as it was.

Fig. 19(a) and (b) compare the simulated and experimental results of the undrained shear tests from CU1-1 to CU1-5 for the effective stress path and the stress-strain relation, respectively. Although there is a scope to enhance the accuracy of the calculation, it is found that the constitutive model with a single set of input parameters for the material can favourably capture the undrained shear behaviours from the different initial conditions as a whole. It is also plausible to assume that the initial stress states of CU1-2 to CU1-5 are normally consolidated because they have approximately similar effective stress paths where the effective mean stress monotonically decreases up to the critical state. Unlike these four cases, the experimental results of CU1-1 indicate that the effective mean stress

Table 2
Initial conditions for the simulation of undrained shear on sodium-type bentonite (Kunigel V1).

Case	Effective mean stress p_i (MPa)	Void ratio* e_i	OCR p_{c0}/p_i
CU1-1	1.00	0.723 (0.723)	1.45
CU1-2	1.49	0.701 (0.702)	1.00
CU1-3	1.96	0.668 (0.663)	1.00
CU1-4	2.43	0.642 (0.651)	1.00
CU1-5	2.92	0.620 (0.615)	1.00

* Within the parentheses is the original value of initial void ratio.

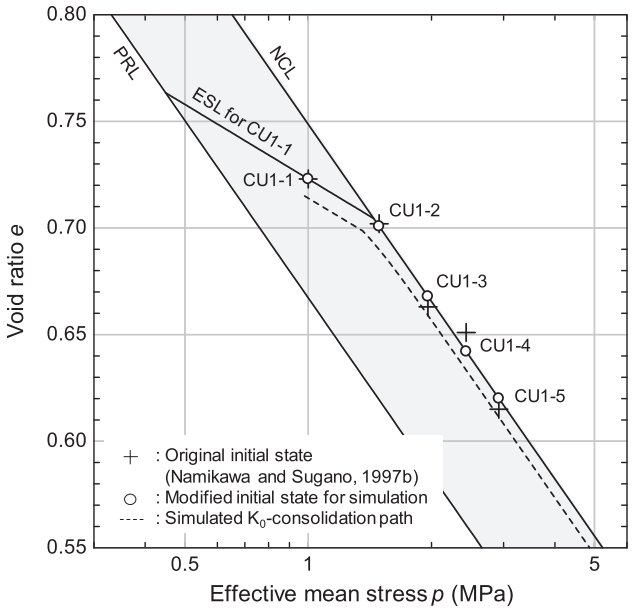

Fig. 18. Initial conditions for simulation of undrained shear tests on sodium-type bentonite.

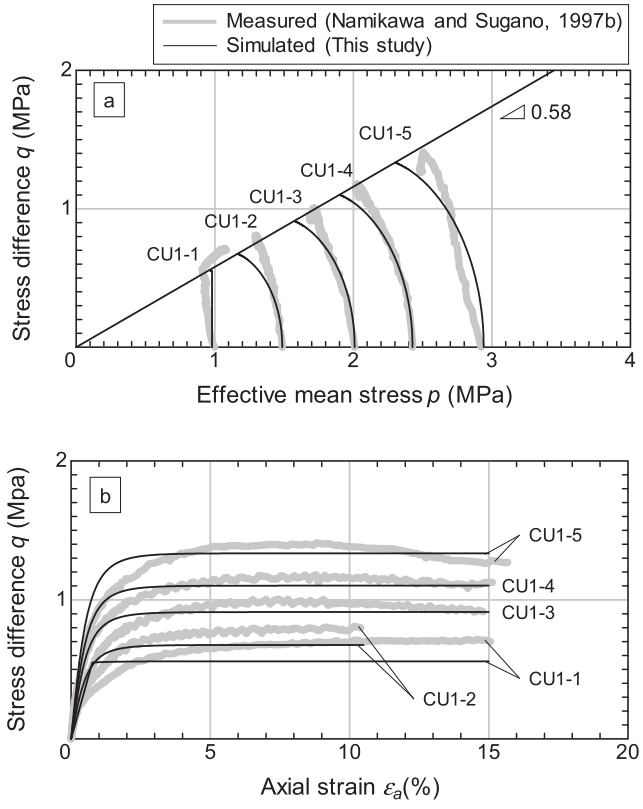

Fig. 19. Comparison of simulated and experimental results of undrained shear tests on sodium-type bentonite (Namikawa and Sugano, 1997b): (a) effective stress path and (b) stress-strain relation.

decreases slightly with an increase in the stress difference and begins to increase near the critical state. On the other hand, the simulated results show no change in the effective mean stress up to the critical state since the initial stress state lies at a point midway between NCL and PRL, as shown in Fig. 18, and the elastic state is maintained during the undrained shear.

4.2. Simulations of laboratory tests on the saturated bentonite-sand mixture

The oedometer and undrained shear tests on the bentonite-sand mixture, of which a sodium-type bentonite occupies 70 mass% conducted by Takaji and Suzuki (1999), will be taken as references for the simulation. As the test procedures were almost similar to those in the preceding section, the details are omitted here.

Table 3 summarizes the parameters adopted for the simulations and Fig. 20 shows the simulated and experimental results of the oedometer test in the $e - \ln\sigma$ plane. The figure reveals the tendency whereby the simulated results gradually digress from the experimental ones as the axial loading progresses, which leads to the overestimation of the decrease in the void ratio at relatively higher stress levels. This is because the NCL is modelled as linear in the $e - \ln p$ plane and compression index λ is estimated based on the experimental results over a relatively lower stress range, in spite of the fact that the NCL of bentonite materials is not linear over a wider stress range even in the $e - \ln p$ plane, as was also pointed out by Kobayashi et al. (2007). The modelling of a curved NCL is an issue that remains to be addressed and improved in addition to the description of the compressibility in the reloading process, as was also mentioned in the preceding section.

Fig. 21 and Table 4 show the initial conditions for the simulation of the undrained shear tests compared with the experimental data. The initial state only in the case of CU2-0 was assumed to be overconsolidated with the OCR value of 1.47, while the rest were normally consolidated. As seen in the figure, it is probably permissible that the NCL is deemed as linear within the stress range dealt with here. Fig. 22(a) and (b) compare the simulated and experimental results for the effective stress paths and the

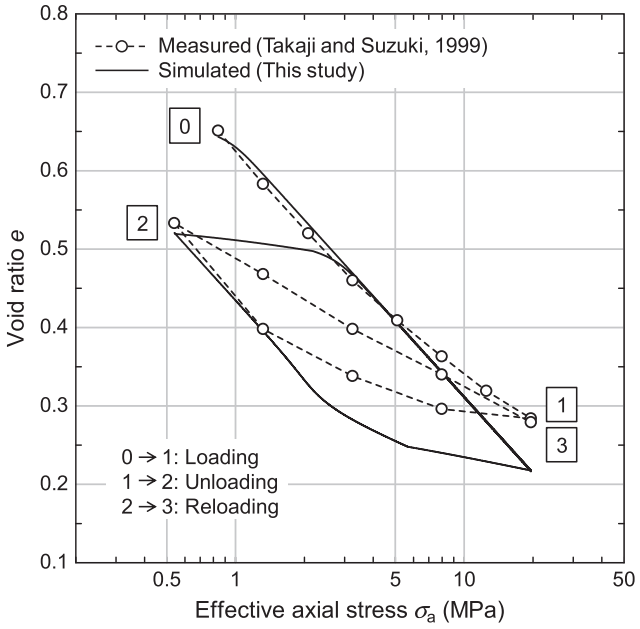

Fig. 20. Comparison of simulated and experimental results of oedometer test on mixture of sodium-type bentonite and silica sand (Takaji and Suzuki, 1999).

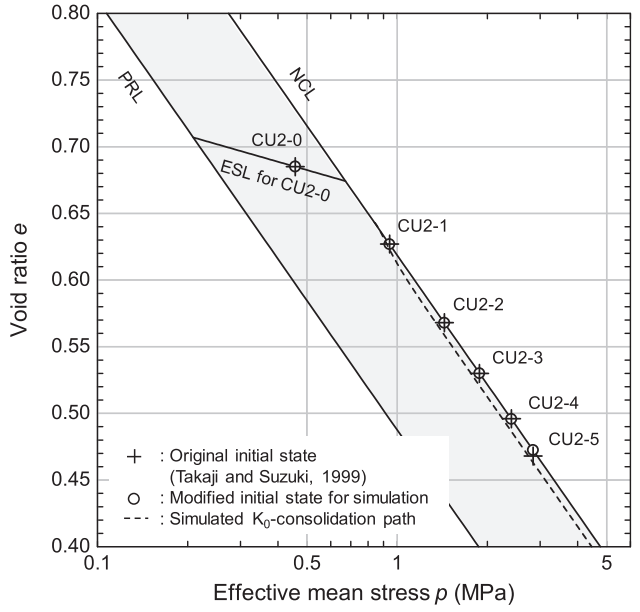

Fig. 21. Initial conditions for simulation of undrained shear test on mixture of sodium-type bentonite and silica sand.

Table 3
Model parameters for the mixture of sodium-type bentonite and silica sand.

λ	Compression index	0.14*
Λ	Irreversibility	0.80*
M	Critical state parameter	0.63**
ζ	Plastic rebound parameter	0.45**
ν	Poisson's ratio	0.40
e_{ref}	Reference combination on NCL	0.64
p_{ref} (MPa)		0.84

* Corresponding value of elastic swelling index: $\kappa = (1 - \Lambda)\lambda = 0.028$.
** Corresponding value of ellipticity: $\tilde{M} = (1 + 2\zeta)M = 1.197$.

stress-strain relation, respectively, from which it is found that the developed constitutive model accurately describes the undrained shear behaviors of the bentonite-sand mixture. Although the case of CU2-0 shows a clearly different effective stress path from those in the cases of CU2-1 to CU2-5, as a result of the experimental tests, the behaviour whereby the effective mean stress changes slightly is expressed as an elastic response in the simulation.

Table 4
Initial conditions for the simulation of undrained shear on the mixture of sodium-type bentonite and silica sand.

Case	Effective mean stress p_i (MPa)	Void ratio* e_i	OCR p_{c0}/p_i
CU2-0	0.457	0.685 (0.685)	1.47
CU2-1	0.943	0.627 (0.627)	1.00
CU2-2	1.437	0.568 (0.568)	1.00
CU2-3	1.882	0.530 (0.530)	1.00
CU2-4	2.405	0.496 (0.496)	1.00
CU2-5	2.840	0.472 (0.468)	1.00

* Within the parentheses is the original value of initial void ratio.

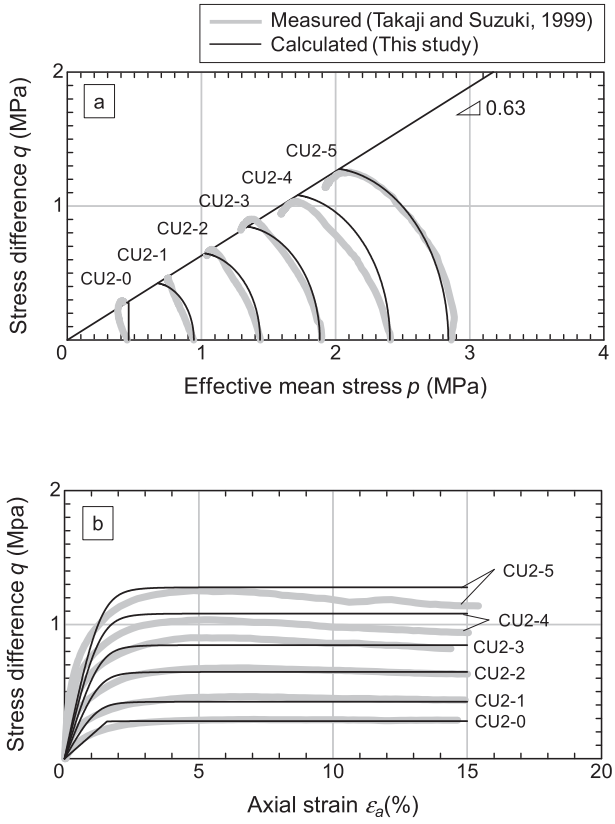

Fig. 22. Comparison of simulated and experimental results of undrained shear tests on mixture of sodium-type bentonite and silica sand (Takaji and Suzuki, 1999): (a) effective stress path and (b) stress-strain relation.

5. Conclusion

A novel constitutive model for expansive soils has been developed in this study which incorporates the concept of plastic rebound into the modified Cam-clay model. To keep the model simple, only one additional parameter has been added to describe the mechanical behaviours of saturated expansive soils. The model not only can provide predictions of the large swelling due to unloading, but can also yield realistic predictions of the effective stress paths for consolidation and swelling in both axial and radial problems, which will contribute to analyses of the generation of swelling pressure and the change in dry density of bentonite buffers.

Analytical investigations in this paper showed the role of the additional parameter related to the plastic rebound in the predictions of consolidation and swelling in axial and radial problems. A close inspection revealed that the magnitude of the additional parameter affected the number of solutions for the convergence condition of $\dot{\eta} = 0$ in each of the axial and radial problems, from which the paper presented a diagram for judging whether a set of model parameters can provide realistic solutions or not. It was also found that the incorporation of the plastic rebound contributed to the obtaining of favourable predictions for the coefficients of earth pressure at rest.

The proposed model improves the predictive capabilities of its parent constitutive model, i.e., the modified Cam-clay model, especially in its description of swelling behaviour. The model will be further improved to encompass both saturated and unsaturated conditions including their transitions.

Acknowledgements

The authors wish to thank Prof. Hideki Ohta, emeritus professor of Tokyo Institute of Technology, for his helpful support and encouragement.

Appendix. The rate and tensorial form of the elastic constitutive relation is given by

$$\dot{\boldsymbol{\sigma}} = \mathbf{c}^{\mathrm{e}} : \dot{\boldsymbol{\varepsilon}}^{\mathrm{e}} = \mathbf{c}^{\mathrm{e}} : (\dot{\boldsymbol{\varepsilon}} - \dot{\boldsymbol{\varepsilon}}^{\mathrm{p}}); \tag{A1}$$

$$\mathbf{c}^{\mathrm{e}} = K\mathbf{1} \otimes \mathbf{1} + 2G\left(\mathbf{I} - \frac{1}{3}\mathbf{1} \otimes \mathbf{1}\right) \tag{A2}$$

where $\mathbf{1}$ is the second-order identity tensor, $\mathbf{c}^{\mathrm{e}}$ is the rank-four elasticity tensor and $\mathbf{I}$ is the rank-four identity tensor denoted such that $\mathbf{I}_{ijkl} = \left(\delta_{ik}\delta_{jl} + \delta_{il}\delta_{jk}\right)/2$ while the symbol $\otimes$ indicates a tensor juxtaposition operator executing such that $(\mathbf{a} \otimes \mathbf{b})_{ijkl} = a_{ij}b_{kl}$ for any second-order tensors $\mathbf{a}$ and $\mathbf{b}$. The elastic bulk and shear moduli, K and G, are formulated such that Eq. (A) involves the invariant constitutive equations of (20) and (21), respectively, as follows:

$$K = \frac{1}{\tilde{M}D}\frac{\Lambda}{1-\Lambda}p \text{ and } G = \mu K. \tag{A3}$$

Assuming the associated flow, the plastic strain rate tensor is obtained as

$$\dot{\boldsymbol{\varepsilon}}^{\mathrm{p}} = \gamma\frac{\partial f}{\partial \boldsymbol{\sigma}} \tag{A4}$$

where γ is the non-negative consistency parameter; and thus, the loading criterion for a plastic flow is given by $\gamma > 0$, while the state becomes elastic when $\gamma = 0$. By applying the consistency condition to the yield function of Eq. (7), into which Eqs. (A1) and (A2) and the hardening law of Eq. (16) are substituted, the consistency parameter can be formulated as

$$\gamma = \frac{1}{H}\frac{\partial f}{\partial \boldsymbol{\sigma}} : \mathbf{c}^{\mathrm{e}} : \dot{\boldsymbol{\varepsilon}};\ H = \frac{\partial f}{\partial \boldsymbol{\sigma}} : \mathbf{c}^{\mathrm{e}} : \frac{\partial f}{\partial \boldsymbol{\sigma}} - \frac{\partial f}{\partial F}\frac{F}{\tilde{M}D}\frac{\partial f}{\partial p}. \tag{A5}$$

Consequently, by substituting Eqs. (A4) and (A5) into (A1), the rate form of the constitutive relation in the elasto-plastic regime is obtained as follows:

$$\dot{\boldsymbol{\sigma}} = \mathbf{c}^{\mathrm{ep}} : \dot{\boldsymbol{\varepsilon}};\ \mathbf{c}^{\mathrm{ep}} = \mathbf{c}^{\mathrm{e}} - \frac{1}{H}\mathbf{c}^{\mathrm{e}} : \frac{\partial f}{\partial \boldsymbol{\sigma}} \otimes \frac{\partial f}{\partial \boldsymbol{\sigma}} : \mathbf{c}^{\mathrm{e}} \tag{A6}$$

Understandably, Eq. (A6) can be reduced to Eq. (24) under the axisymmetric or triaxial condition.

References

Alonso, E.E., Gens, A., 1999. Modelling the mechanical behaviour of expansive clays. Eng. Geol. 21, 173–183.

Amerashinghe, S.F., Kraft, L.M., 1983. Application of a Cam-clay model to overconsolidated clay. Int. J. Numer. Anal. Meth. Geomech. 7, 173–186.

Bjerrum, L., 1967. The progressive failure in slopes of overconsolidated plastic clay. Soil Mech. Found. Eng. Div., ASCE 93, 3–49.

Börgesson, L., Johannesson, L.-E., Sanden, T., Hernelind, J., 1995. Modelling of the physical behaviour of water saturated clay barriers. Svensk Kärnbränslehantering AB.

Börgesson, L., Karland, O., Johannesson, L.E., 1996. Modelling of the physical behavior of clay barriers close to water saturation. Eng. Geol. 41, 127–144.

Calabresi, G., Scarpelli, G., 1985. Effects of swelling caused by unloading in overconsolidated clays. Proc. of 11th International Conference on Soil Mechanics and Foundation Engineering, pp. 411–414.

Carter, J.P., Booker, J.R., Wroth, C.P., 1982. A critical state soil model for cyclic loading. In: Pande, G.N., Zienkiewicz, O.C. (Eds.), Soil Mechanics – Transient and Cyclic Loads. Johnson Wiley & Sons Ltd., pp. 219–252.

Cui, Y.J., Yahia-Aissa, M., Delage, P., 2002a. A model for the volume change behavior of heavily compacted selling clays. Eng. Geol. 64, 233–250.

Cui, Y.J., Loiseau, C., Delage, P., 2002b. Microstructure changes of a confined swelling soil due to suction controlled hydration. Proc. of the 3rd International Conference on Unsaturated Soils, Recife 2, 593–598.

Cui, Y.J., Nguyen, X.P., Tang, A.M., Li, X.I., 2013. An insight into the unloading/reloading loops on the compression curve of natural stiff clays. Appl. Clay Sci. 83–84, 343–348.

Cui, Y.J., 2017. On the hydro-mechanical behaviour on MX80 bentonite-based materials. J. Rock Mech. Geotech. Eng. 9, 565–574.

Dueck, A., Börgesson, L., Johannesson, L.-E., 2010. Stress-strain relation of bentonite at undrained shear. Svensk Kärnbränslehantering AB.

Dueck, A., Goudarzi, R., Börgesson, L., 2016. Buffer homogenisation: status report 3. Svensk Kärnbränslehantering AB.

Gens, A., Alonso, E.E., 1992. A framework for the behavior of unsaturated expansive clays. Can. Geotech. J. 29, 1013–1032.

Hashiguchi, K., 1980. Constitutive equations of elastoplastic materials with elastic-plastic transition. J. Appl. Mech. 47, 266–272.

Hashiguchi, K., 1989. Subloading surface model in unconventional plasticity. Int. J. Solids Struct. 25, 917–945.

Hashiguchi, K., Mase, T., 2007. Extended yield condition of soils with tensile strength and rotational hardening. Int. J. Plast. 23, 1939–1956.

Hoffmann, C., Alonso, E.E., Romero, E., 2007. Hydro-mechanical behaviour of bentonite palette mixture. Phys. Chem. Earth. 32, 832–849.

Jaky, J., 1944. The coefficient of earth pressure at rest. J. Soc. Hungarian Architects Eng. 7, 335–358 (in Hungarian).

Jaky, J., 1948. Earth pressure in silos. Proceedings of the 2nd International Conference on Soil Mechanics and Foundation Engineering 1, 103–107.

Jones, L.D., Jefferson, I.F., 2012. Expansive soils. In: Burland, J. (Ed.) ICE manual of Geotechnical Engineering. Vol. 1, Geotechnical Engineering Principles, Problematic Soils and Site Investigation. ICE Publishing, London, UK, pp. 413–441.

Kobayashi, I., Toida, M., Sasakura, T., Ohta, H., 2007. Interpretation of compression/swelling behavior of compacted bentonite using constant water-content line and constant degree-of-saturation line. J. JSCE III 63 (4), 1065–1078 (in Japanese).

Komine, H., Watanabe, Y., 2010. The past, present and future of the geo-environment in Japan. Soils Found. 50 (6), 977–982.

Lloret, A., Villar, M., Sánchez, M., Gens, A., Pintado, X., Alonso, E.E., 2003. Mechanical behaviour of heavily compacted bentonite under high suction changes. Géotechnique 53 (1), 27–40.

Manca, D., Ferrari, A., Laloui, L., 2016. Fabric evolution and the related swelling behaviour of a sand/bentonite mixture upon hydro-chemo-mechanical loadings. Géotechnique 66, 41–57.

Mitachi, T., 2008. Mechanical behavior of bentonite-sand mixtures as buffer materials. Soils Found. 48 (3), 363–374.

Mroz, Z., 1967. On the description of anisotropic workhardening. J. Mech. Phys. Solids 15, 163–175.

Namikawa, T., Sugano, T., 1997a. Consolidation properties of buffer material. Report of Power Reactor and Nuclear Fuel Development Corporation, PNC TN8410, 97–151 (in Japanese).

Namikawa, T., Sugano, T., 1997b. Shear properties of buffer material I. Report of Power Reactor and Nuclear Fuel Development Corporation, PNC TN8410, 97–174 (in Japanese).

Parry, R.H.G., Amerasinghe, S.F., 1973. Components of deformation in clays. Proc. Symp. Role Plast. Soil Mech., 108–126

Pusch, R., 1979. Highly compacted sodium bentonite for isolating rock-deposited radioactive waste products. Nucl. Technol. 45 (2), 153–157.

Pusch, R., 1982. Mineral water-interaction and their influence on the physical behaviour of highly compacted Na bentonite. Can. Geotech. J. 19, 381–387.

Romero, E., Simms, P.H., 2008. Microstructure investigation in unsaturated soils: a review with special attention to contribution of mercury intrusion porosometry and environmental scanning electron microscopy. Geotech. Geol. 26 (6), 705–727.

Roscoe, K.H., Burland, J.H., 1968. On the generalized stress-strain behavior of 'wet' clay. In: Heyman, J., Leckie, F.A. (Eds.), Engineering Plasticity. Cambridge Univ. Press, pp. 535–609.

Sasakura, T., Kuroyanagi, M., Kobayashi, I., Okamoto, M., 2003. Studies on mechanical behaviour of bentonite for development of the constitutive model II. Report of Japan Nuclear Cycle Development Institute, JNC TJ8400 2003-048 (in Japanese).

Seiphoori, A., Ferrari, A., Laloui, L., 2014. Water retention behaviour and microstructural evolution of MX-80 bentonite during wetting and drying cycles. Geotechnique 64 (9), 721–734.

Shibata, T., 1963. On the volume change of normally consolidated clays. Disaster Prevention Research Institute Annuals, Kyoto University, 128–134.

Suebsuk, J., Horpibulsuk, S., Liu, M.D., 2011. A critical state model for overconsolidated structured clays. Comput. Geotech. 38, 648–658.

Sun, W., Sun, D., 2012. Coupled modelling of hydro-mechanical behaviour of unsaturated compacted expansive soils. Int. J. Numer. Anal. Meth. Geomech. 36, 1002–1022.

Takahashi, A., Fung, D.W.H., Jardine, R.J., 2005. Swelling effects on mechanical behaviour of natural London Clay. Proc. of 16th International Conference on Soil Mechanics and Geotechnical Engineering 2, 443–446.

Takaji, K., Suzuki, H., 1999. Static mechanical properties of buffer material. Report of Japan Nuclear Cycle Development Institute, JNC TN8400 99-041 (in Japanese).

Terzaghi, K., 1936. Stability of slopes of natural clay. Proc. 1st International Conference on Soil Mechanics and Foundation Engineering 1, 161–165.

Takayama, Y., Tsurumi, S., Iizuka, A., Kawai, K., Ohno, S., 2012. An interpretation of mechanical properties of bentonite as a non-linear elastic material. Int. J. GEOMATE 3 (2), 357–362.

Takayama, Y., Tachibana, S., Iizuka, A., Kawai, K., Kobayashi, I., 2017. Constitutive modeling for compacted bentonite buffer materials as unsaturated and saturated porous media. Soils Found. 57, 80–91.

Tong, F., Yin, J.H., 2011. Nonlinear creep and swelling behavior of bentonite mixed with different sand contents under oedometric condition. Mar. Georesour. Geotechnol. 29 (4), 346–363.

Yong, R.N., Boonsinsuk, P., Wong, G., 1986. Formulation of backfill material for a nuclear fuel waste disposal vault. Can. Geotech. J. 23 (2), 216–228.

Yong, R.N., 1999. Overview of modeling of clay microstructure and interactions for prediction of waste isolation barrier performance. Eng. Geol. 54, 83–91.

Villar, M.V., Lloret, A., 2004. Influence of temperature on the hydro-mechanical behaviour of a compacted bentonite. Appl. Clay Sci. 26 (1–4), 337–350.

Wood, D.M., 1990. Soil Behaviour and Critical State Soil Mechanics. Cambridge University Press.